



UNIVERSITÀ POLITECNICA DELLE MARCHE
Repository ISTITUZIONALE

Long-term evolution of an inner bar at the mouth of a microtidal river

This is the peer reviewed version of the following article:

Original

Long-term evolution of an inner bar at the mouth of a microtidal river / Baldoni, A.; Perugini, E.; Soldini, L.; Calantoni, J.; Brocchini, M.. - In: ESTUARINE, COASTAL AND SHELF SCIENCE. - ISSN 0272-7714. - 262:(2021). [10.1016/j.ecss.2021.107573]

Availability:

This version is available at: 11566/298934 since: 2024-04-30T08:41:05Z

Publisher:

Published

DOI:10.1016/j.ecss.2021.107573

Terms of use:

The terms and conditions for the reuse of this version of the manuscript are specified in the publishing policy. The use of copyrighted works requires the consent of the rights' holder (author or publisher). Works made available under a Creative Commons license or a Publisher's custom-made license can be used according to the terms and conditions contained therein. See editor's website for further information and terms and conditions.

This item was downloaded from IRIS Università Politecnica delle Marche (<https://iris.univpm.it>). When citing, please refer to the published version.

(Article begins on next page)

“Long-term evolution of an inner bar at the mouth of a microtidal river”

Agnese Baldoni^a, Eleonora Perugini^a, Luciano Soldini^a, Joseph Calantoni^b, Maurizio Brocchini^a

^aUniversità Politecnica delle Marche, Ancona, Italy.

^bOcean Sciences Division, U.S. Naval Research Laboratory, Stennis Space Center, MS, USA.

Corresponding author: Agnese Baldoni (a.baldoni@pm.univpm.it)

Abstract

We conducted, for the first time, a study of the long-term evolution of an inner mouth bar in a microtidal environment that complements field observations with detailed numerical modelling of the same morphodynamics. Images collected by a video-monitoring station, from 2016 to 2019, were processed to study the evolution of a persistent inner mouth bar formed inside the highly engineered Misa River estuary (Senigallia, Italy) after years of reduced precipitation and discharges. We developed a semi-automatic procedure to detect the emerged area of this deposit. We seek to quantify the relationship between the long-term evolution of the bar and the forcing from the river, waves and tides. The observed high peaks in river discharge caused a strong downriver bar migration (i.e. [almost twice the river width](#)). Conversely, the observed [sea](#) storms produced an upriver bar migration [smaller than one river width](#). A much slower and weaker (less than half the [river width](#)) upriver migration was also observed during periods of large area accretion and [due to](#) mild wave climate. Moreover, results showed that the [sea water level variation](#) did not directly impact the morphodynamics of the estuary, [affecting the emerged portion of the bar only](#). Numerical simulations, run with Delft3D, were used to complete the information coming from field observations. After some checks on the proper use of the solver for the scenarios and environments of interest, some parametric simulations were run to highlight the role of the different forcing on the bed evolution. Simulations showed, as expected, erosion of the riverbed and significant downriver migrations (four river widths) during peaks of river discharge comparable to the 1-year return period discharges. Numerical results also showed upriver sediment transport when the wave forcing was dominant, with 10-years return period waves inducing an upriver bar migration in the order of one river width. Then, one real-life event was simulated to inspect the interaction of the various forcing and to compare their effects with the observations. Our analysis provides new insight into the complex morphodynamics in a microtidal estuary when weak river discharge is opposed by sea waves driving upriver sediment transport. A more thorough understanding of the morphodynamics is needed for future forecasting of the formation and evolution of sediment deposits inside estuarine channels that can inhibit both navigation and the flux of sediment from the river to the estuary.

Key words: mouth bar, microtidal estuary, morphodynamics, river-wave interaction, video monitoring, image processing

1

2

3

1. Introduction

The river mouth is a complex area characterized by the interaction between the forces of the sea (wave and tidal) and the discharge of the river. The morphodynamics of this environment is often characterized by the formation of sand bars and shoals as a result of the relative role of the different factors that influence the sediment transport. Previous studies largely focus on the formation of a typical mouth bar (sediments deposited by flow expansion, out of the mouth at a distance of about twice the river width, e.g. [Fagherazzi et al., 2015](#)), the evolution of river bars (not influenced by waves and tides, e.g. [Blondeaux and Seminara, 1985](#); [Colombini et al., 1987](#)), and the evolution of tidally controlled systems (e.g. [Hayes, 1980](#), [Dalrymple and Choi, 2007](#)). However, the scenario of an inner mouth bar in a microtidal environment subject to strong wave action has not been extensively studied.

From a mechanical point of view, downriver sediment transport in wave-dominated, microtidal estuaries may lead to various deposition scenarios ([Wright, 1976](#)). The flow slow down due to the sudden expansion of the cross-section of water debouching in the sea (e.g., [Mikhailov, 1966](#)) and of the relative strength of the downriver flows (weak or sustained rainfalls) to upriver flows (e.g. sea waves and tidal currents, see [Chawla & Kirby, 2002](#)) both drive gradients in sediment transport rates leading to deposition. Additional controlling mechanisms are bed friction and buoyancy, the latter still largely unexplored ([Fagherazzi et al., 2015](#)). However, the evolution of wave-dominated river mouths has been documented recently ([Anthony, 2015](#); [Brocchini, 2020](#)).

Typical scenarios evolve over an annual cycle characterized by 1) the expulsion of sediment out of the river mouth because of the intense rain-driven river water jet, typically in winter, and 2) sediment accumulation, usually in summer, because of the weak river flows and continuous action of upriver flows due to waves and modulating tides ([Brocchini et al., 2017](#)). The dynamics of the downriver sediment transport are largely controlled by the stability of the river water jet ([Canestrelli et al., 2014](#)); in frictionally dominated flows characterized by a large stability number, the flow rapidly spreads, causing a fast decrease in centreline velocity, thus forming a prominent mouth bar and short and rapidly diverging levees. On the contrary, pronounced levees and elongated channels are formed for low stability numbers. Also, it has been shown that lateral advection and diffusion of suspended sediment are directly proportional to jet potential vorticity; large sediment potential vorticity fosters levee deposition (channel elongation in the sea), while small potential vorticity encourages mouth bar deposition ([Falcini et al., 2014](#)). Hence, the most typical morphological scenarios are characterized by either an inner river bar, or an outer river bar (typically at a distance of twice the mouth width), or a more spread deposition pattern out of the river mouth, at times giving a shoal type bathymetry (e.g. [Olabarrieta et al., 2014](#)).

Motivated by some recent detailed video monitoring observations of the riverbed morphology at the Misa River (Senigallia, Italy), we have focused on the mechanisms that characterize the evolution of a persistent inner river mouth bar displayed in Figure 1. The bar emerged above the mean water level in 2016 and spanned much of the river mouth cross section. The bar is largely constituted by coarse sediments (very coarse sand and gravel) lying over a layer of much finer muddy sediments (silt and clays).



Fig. 1. Images of the bar formed inside the mouth of the Misa River.

Traditional “in-situ” topographic and bathymetric survey techniques provide detailed measurements of the area surrounding the river bar; while these techniques may be executed readily during dry periods, they are inhibited by the adverse conditions present during flood events. In the last decades, the use of remote sensing was largely developed as an alternative to “in-situ” surveys. A detailed review of the use of remote sensing in various studies in the nearshore area was given by [Holman and Haller \(2013a\)](#). Many sensors and platforms are available, but fixed optical cameras and X-band radar still represent the most frequently used and best developed. Also, satellite images have become a powerful instrument following the wide availability of high-quality commercial imagery. An important role is played by the resolution of the phenomenon in time and space. Use of satellite images permits synoptic analyses over wide areas and long-time scales. For example, coastal morphodynamics are reconstructed in the estuary area of the Red river system, Vietnam, over the period of 1975 to 2009, using satellite images ([Thi Lan et al., 2013](#)). On the ground, images obtained from fixed optical cameras or X-band radar may provide optimal data for high resolution analyses in time and space. [Takewaka \(2016\)](#) showed the morphological changes of a river sand bar during a flood event with X-band marine radar data collected continuously for 72 hours. [Pianca et al. \(2014\)](#) analysed the evolution of the bedforms of an ebb delta over 23 days using snapshots and post processed images collected by six fixed video cameras. Moreover, the high-resolution video cameras combined with well-known techniques for image analysis ([Holman and Stanley, 2007](#); [Holman et al. 2013b](#); [Perugini et al., 2019](#)) permit the study of both emerged and submerged morphology. Finally, a Particle Tracking Velocimetry (PTV) technique can be applied to the videos to study the hydrodynamics of the river mouth.

Optical images collected from July 2015 to December 2019 at the Misa River demonstrate the potential of the fixed cameras in both short and medium-term analyses. Optical imagery collected by a dedicated video monitoring station during daylight hours is used to describe the evolution of the river sand bar, that can vary both rapidly and slowly in space and time. The characteristics of the studied area, of the monitoring station and all other observations are described in Section 2, including the technique used for post-processing the videos and extracting the river bar evolution. Section 2 also describes the numerical simulation used to analyse the observed morphodynamics. The results of both field observations and numerical simulation are summarized in Section 3. Discussion and conclusions are given in Section 4 and Section 5, respectively.

2. Methods

2.1. Regional setting and instrumentation

The study area is around the Misa River (MR hereinafter) estuary, within the town of Senigallia, located in the Italian Middle Adriatic coast. The watershed of the MR is 383 km², with a discharge of about 400 m³/s for a return period of 100 years. The MR estuary is

classified as a salt-wedge estuary, characterized by freshwater flowing out to the sea in the upper layer of the water column and a seawater intrusion occurring in the lower layer ([Valle-Levinson, 2010](#)). Moreover, the MR estuary is subject to micro-tidal oscillations (mean tidal range less than 0.6 m) with the river forcing typically dominating both the actions of waves and tide.

Like other rivers originating in the Apennine Mountains, the MR is also characterized by large sediment transport rates despite its moderate discharge. The abundance of sediment load is due to the characteristics of the sedimentary rocks that constitute the Apennine Mountains, which are brittle and heavily fractured, thus easily erodible. [This leads to the formation of mouth bars in the MR, as in all Adriatic rivers, even with very different geometrical configurations and structural constraints.](#) Sediment supply consists of limestone, shale, and sandstone. Moreover, the deposition of volcanic ash, transported from the southeast by winds during the Plinian and other volcanic eruptions (e.g. [Rolandi et al., 2008](#)), has added an abundant quantity of montmorillonite clays to this mix of minerals. Sediment cores, collected by [Favali et al. \(1995\)](#) in the alluvial layers underlying the town of Senigallia, displayed layers of muddy sediments, interspersed with gravel, all of which overlie the bedrock of fractured and faulted mud-, silt- and sandstone. Consequently, the MR is a suitable location to study the evolution of the morphodynamics caused by the effects of river discharge and nearshore hydrodynamics. Moreover, the final reach of the MR is comparable to a field-scale laboratory flume (e.g. [Brocchini et al., 2017](#); [Melito et al., 2020](#)) since it flows within a fixed engineered channel [of approximate width of 25-30 m](#). The beach to the north of the MR estuary is engineered with breakwaters, while the beach to the south is a natural open coast.

The Sena Gallica Speculator (SGS) video-monitoring station is located at the north pier of the Senigallia harbour. SGS contains four cameras located on the top of a tower about 25 m above mean sea level. Three cameras face South, toward the 500 m long unprotected beach between the harbour jetty and the Rotonda pier; the fourth camera faces northward, toward the estuary of the MR (Figure 2a). For each recording hour, the data collected from each camera consist of a ten-minute video (collected at 2 Hz) and a snapshot. The acquisition occurs during daylight hours, from 5:00 AM to 5:00 PM UTC, for a total of thirteen videos and thirteen snapshots a day, for each camera ([Perugini et al., 2018](#); [Perugini, 2019](#)).

The hourly videos and snapshots recorded from the SGS station are post-processed to create a range of remotely sensed products. One of the products of the post-processing is an orthorectified, time exposure, stabilized plan-view image for each recording hour. First, the videos of each hour and each camera are used to create a 10-minute time-exposure image (Timex) by averaging the intensity values of each pixel over the 10-minute sampling period. Image stabilization is utilized for each hour and each camera. The geometric transformation between the analysed Timex and the Timex image of the day when the camera geometry has been calculated (target Timex) is estimated and applied to the analysed image. Then the oblique and stabilized Timex images are geo-rectified using a photogrammetric method (based on [Hartley and Zisserman, 2003](#)), which allows for the transformation from image (2D) to world (3D) coordinates by fixing one of the real coordinates, generally the z-coordinate equal to the measured tidal level. In this case, since the MR estuary is microtidal, the z-coordinate is assumed to be equal to zero. For each hour, the four ortho-rectified Timex images are merged to obtain the plan view image. All the post-processing operations have generated a continuously updated database since July 2015. The plan-view images, from 2016 to 2019, were processed to detect a bar formed in the final reach of the MR. For each day, a

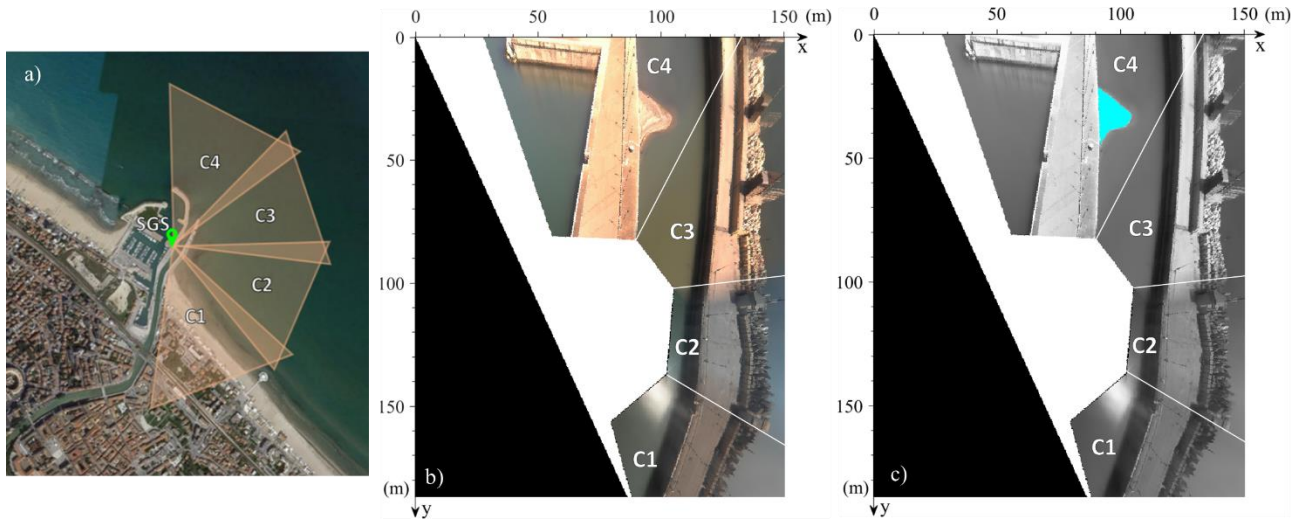


Fig. 2. a) Position of the SGS Station in the Senigallia harbour and the cameras field of view (total field of view 200°, resolution between 0.05 m and 50 m). C1, C2, C3 and C4 are the camera names. b) RGB cropped and rotated image, with its reference system in meters and the cameras field of view. c) Grayscale image, with the result of the detection of the bar superimposed (cyan) and the cameras field of view.

set of thirteen plan-view images, with size 3667×2401 pixels, were available. The database also provides the world coordinates of the pixels of each image in WGS84. To observe the effect of different forcing on the evolution and migration of the bar, several additional observations were included in this study.

Wave climate data were collected by an offshore ADCP, (<http://www.morse.univpm.it>), located within the Meda station (CNR-IRBIM), which is about 1.5 nautical miles north of Senigallia and 1.5 nautical miles offshore. The ADCP recordings of wave height and direction started on 8 August 2018. For previous periods, the wave climate was derived from the Mediterranean Sea Waves Hindcast of the Copernicus Programme; the CMEMS multi-year wave hindcast started from February 2006 and was composed of hourly wave parameters at 1/24° horizontal resolution, covering the Mediterranean Sea and extending up to -18.125W into the Atlantic Ocean. It is produced by the Mediterranean Sea Waves forecasting system, a wave model based on WAM Cycle 4.5.4, which has been developed as a nested sequence of two computational grids (coarse and fine) to ensure that swell propagating from the North Atlantic towards the strait of Gibraltar is correctly entering the Mediterranean Sea (CMEMS, Copernicus). The resolution of the whole set of data is one datum per hour.

The river water level was collected by a hydrometer, located at “Ponte Garibaldi”, every 30 minutes. The gauge was installed in 2016 by the Civil Protection of the Marche Region at a distance of about 1.5 km from the MR mouth. Since the local datum of the river gauge is on the riverbed, its data can be taken to be the water column elevation at that specific location.

Data of river discharge were harder to obtain. Rating curves of “Bettolelle”, a Civil Protection hydrometer located about 10 km from the MR estuary, were used to compute the river discharge whenever possible. For example, curves were available for the periods 23 March 2015 - 5 March 2018 and 15 – 31 December 2019. The dataset provided one datum every 30 minutes. In order to extend the dataset for use by the simulation, discharge data were added from 6 March 2018 to 16 December 2019 using the curve valid until 5 March 2018.

The sea water level was derived from the ISPRA Tide Station installed inside the Ancona Harbour, about 25 km away from Senigallia. Another set of data starting in July 2018 was available from a tide gauge (<http://www.morse.univpm.it>) located within a protected area close to the entrance of Senigallia harbour. Since the relative changes in observed elevations between the two recorded signals were in good and continuous agreement, it was decided to use the sea water level of the Ancona gauge. The Ancona harbour tide gauge records water level data at a frequency of 0.1 Hz and its elevation datum is the mean sea level.

The water level recordings from the Ancona gauge were analysed, using the Delft3D TIDE module, to separate the astronomical contribution from the meteorologically-induced fraction of the observation.

2.2. Video observations

The plan-view images were processed to detect the bar and automatically measure its emerged area (hereinafter simply “area”) and centre of mass. The reference frame in use is displayed in Figure 2b, and it was obtained by cropping the orthorectified plan-view image and rotating it around the origin by 24.8°. The resulting reference frame has the y-axis in the long-river direction, positive upriver, and the x-axis in the cross-river direction, positive rightward (or eastward). Figure 2b also shows that, for a small reach of the river, not the whole cross section is framed by the cameras, because of their installation height and tilt. Considering that the bar was almost always adjacent to the west bank of the river, a portion of it was not visible when its position fell above 82 m, relative to the y-axis of the reference system shown in Figure 2b.

We need to emphasize that a zero value for the area of the bar does not imply that the bar was not emerged. In fact, there were situations when the area of the bar was set equal to zero (e.g., when the meteorological lighting conditions were insufficient to identify the bar, when the position of the bar fell out of the field of view, or when the SGS station was inoperable. The first step of the procedure consisted of cropping and converting the images to grayscale to focus on the river mouth. Only images that showed the presence of the bar were analysed further. A mask was applied to the cropped image, 801×501 pixels, to exclude all areas except for the final reach of the MR. In the next step a Region Of Interest (ROI) was defined, i.e. a window inside the image where the detection of the bar was performed. The ROI had to be changed and adapted for each analysed day. Then the gradient of the image was performed, using the Sobel gradient operator, which computes the gradient of a pixel as a weighted sum of pixels in its 3-by-3 neighbourhood. The weights for gradients in the vertical direction are

$$\begin{bmatrix} 1 & 2 & 1 \\ 0 & 0 & 0 \\ -1 & -2 & -1 \end{bmatrix}. \quad (1)$$

For the horizontal direction, the weights are transposed. The resulting gradient image was converted into binary format that either (1) produced a suitable image for the final identification of the bar or (2) produced a totally black image. In the first case, the bar was detected and overlaid on the grayscale image to allow the user to check the result (Figure 2c). In the second case, contrast enhancement was performed on the original image and the gradient of the image operation was repeated. In most cases, the failure to make a suitable binary image resulted from insufficient image contrast, which prevented the gradient operation from identifying the bar. The contrast

was improved using Contrast Limited Adaptive Histogram Equalization (CLAHE). Adaptive Histogram Equalization (AHE) differs from ordinary histogram equalization methods because it computes several histograms, each corresponding to a distinct section (or tile) of the image. Consequently, local contrast is improved by enhancing the definitions of edges in each region of the image. However, AHE tends to amplify the noise in relatively homogeneous regions of the image, therefore CLAHE was used to limit such amplification, by clipping the histogram at a predefined value (Zuiderveld, 1994). The CLAHE algorithm was used whenever the first attempt to identify the bar failed. So, the detection of the bar could be executed with two different sequences of image-processing operations, and the best result could be accepted. If both methods failed to recognize the bar, the user could discard both results and draw the bar shape manually. Once the bar boundaries were identified, the area of the bar and its centre of mass were computed by counting the number of pixels in the detected region. Figure 3 reports the flow-chart of the algorithm, which is available online (<https://github.com/Coastal-Imaging-Research-Network/River-Bar-Toolbox>).

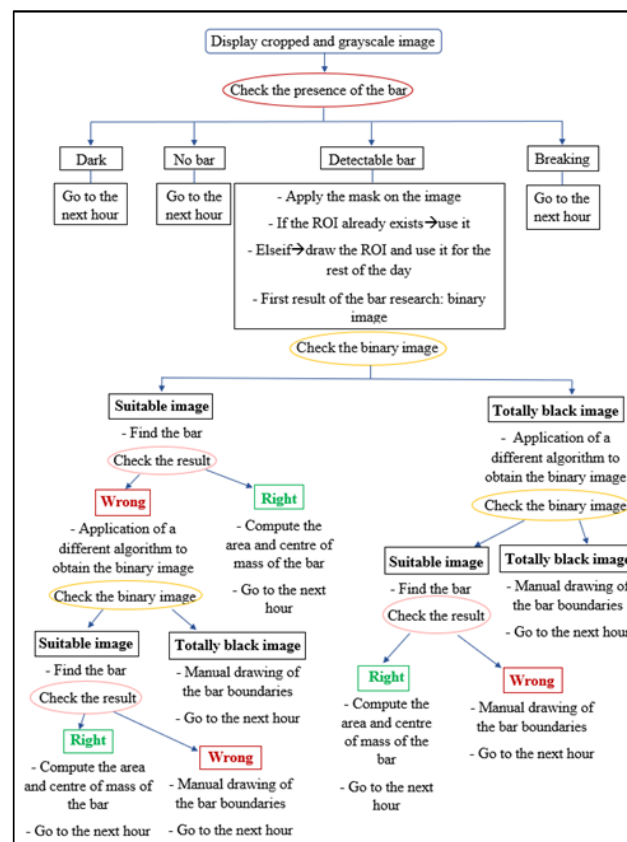


Fig. 3. Flow-chart of the algorithm.

The conversion between pixel and meters was done comparing the image and the world coordinates (WGS84-UTM) of the plan-view images. The resulting scale factor was 0.2999 m/pixel.

During a single day, the observed area of the bar would change due to tidal variations. Since we were not interested in the hourly effect of the tide, we extracted a single datum per day. In order to obtain representative values of the area and centre of mass of the bar for each day, a mean of the daily data was computed. For each day, data from 5:00 AM to 5:00 PM were averaged with an arithmetic mean.

1 2.3. Numerical modelling

2 A two-dimensional (2D), depth-averaged, model was set-up using the Delft3D software suite ([Deltares, 2014](#); [Deltares, 2019](#)) to
3 simulate an observed event and to analyse the effect of different forcing through parametric simulations. Three regular grids were
4 created. The largest grid covered the coastal area in front of the Senigallia Harbour. It had a resolution of 33.3 m and extended about 7
5 km in the alongshore direction and 2.5 km in the offshore direction. The grid was rotated by 47.6° with respect to the North, to follow
6 the coast orientation. The intermediate-size grid was created from the largest one by cutting some cells at the offshore and lateral
7 boundaries. It extended about 6 km in the alongshore direction and 2.4 km in the cross-shore direction. The finest grid covered the final
8 stretch and the mouth of the MR and expanded about 1 km in alongshore direction and 1.5 km in the offshore direction. It had a variable
9 resolution ranging from around 8.3 m in the offshore region to around 3.0 m along the river. The reference system was Monte Mario /
10 Italy Zona2 (Figure 4a).

11 In the offshore region, the bathymetry was created by interpolating the values from the EMODnet bathymetry, available online, at the
12 grid nodes. The bathymetry for the nearshore was built out of a multibeam echosounder survey performed in September-October 2018.
13 It covered the final reach of the MR and the coast both north and south of the harbour. It showed the presence of a submerged deposit,
14 some 60 cm under the water surface. In fact, reduced river discharges, occurring over the last 3-4 years, have led to the stable presence
15 of a sediment deposit (the bar) within the river mouth, continuously evolving. The riverbed was described using two layers of sediments,
16 the upper one, with variable thickness, used to model the shape of the deposit, while the lower one with constant thickness. The
17 sediments have been characterized using the results of two monitoring campaigns, one of April 2019, interesting the final stretch of the
18 MR, and one of February 2018, representative of the beach to the south of the MR ([DHI report, 2020](#)). The results of these campaigns
19 show that the riverbed is mainly composed of silts and clays, with a progressive amount of sand moving toward the mouth, where also
20 gravel is present. Considering this, the bed was composed of both cohesive sediment and sand. The sand was characterized by a median
21 diameter of 180 µm, while for the cohesive sediment we used a critical shear stress for erosion of 0.3 N/m², a critical shear stress for
22 deposition of 0.4 N/m², a settling velocity of 0.1 mm/s and an erosion parameter of 10⁻⁴ kg/m²/s (e.g., [van der Wegen, 2010](#); [Witting et al., 2010](#)).
23 The percentages of cohesive sediment and sand were varied, respectively, by progressively increasing the sand fraction
24 downstream of the most upriver section (in the following “river section”), located 600 m upriver from the mouth, where the bed was
25 composed of cohesive sediment only, to the sea, where the bed was composed only of sand. This was valid for both the upper and
26 lower layers. In addition, in correspondence of the bar, the upper layer had a 5% increase of gravel (median diameter = 6000 µm), with
27 an equivalent reduction of sand. This composition well-represented also the mixture of sediments found in the samples collected in the
28 final 620 m of the MR during the EsCoSed project, showing highly heterogeneous sediments, with a mix of gravel, mud and sand
29 ([Brocchini et al., 2017](#)).

30 Delft3D-FLOW ([Deltares, 2014](#)) was online coupled with Delft3D-WAVE ([Deltares, 2019](#)). The boundary conditions were chosen to
31 reproduce as closely as possible the field forcing conditions. In particular, the WAVE module was forced using recorded timeseries of
32 wave parameters. The input data were applied at the seaward boundary of the largest grid. Then, we nested the smallest grid in the
33 largest grid to obtain a proper propagation of the waves near the harbour and the estuary, thanks to the finer resolution of the smallest

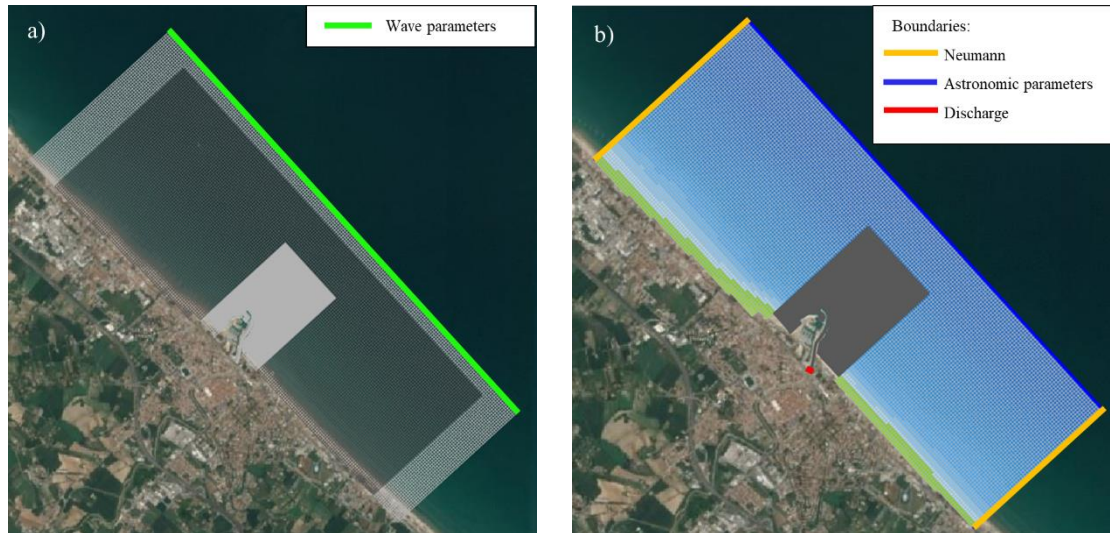


Fig. 4. a) Overview of the three numerical simulation grids and location of the boundary for the WAVE simulation. b) Location of the boundaries and boundary conditions for the FLOW simulation.

grid. The FLOW module was run on the intermediate-size and in the finest grid through the Domain Decomposition approach. It was forced using river discharge, water level boundary conditions, and the results of the WAVE module. The discharge timeseries was used for the river boundary. The amplitude and phase of the Ancona tidal components were specified at the seaward boundary while a zero-water level gradient (Neumann) was set at the cross-shore boundaries. A reflection coefficient was imposed at the offshore boundary to obtain weakly reflective conditions (Figure 4b).

Simulations were run to separately observe the effect of the river flow (R) and of the waves (W) on the bar. In the R cases, artificial flood hydrographs, which reproduce the shape of typical MR flood hydrographs with peak discharges comparable to the 1-year return period discharges, were built and used as input in the river section of the domain. The wave process was turned off to observe the river current action only. On the contrary, for the W cases, the river discharge was set to a very low constant value, $5 \text{ m}^3/\text{s}$, and two artificial storms were created, following the shape of typical NNE and E storms with peak storm significant heights comparable to the 10-years return period heights, to observe the effects of the waves only. Moreover, these simulations were run with and without adding the astronomical tide at the offshore boundary, to understand whether the role of the tide is important for the bar evolution.

In addition, a numerical simulation aimed at observing the combination of all the forcing was also run. The inputs were observed timeseries of river discharge and waves and the astronomical tide. The simulated period was 18 March 2018-1 April 2018.

2.3.1 An assessment of the proper use of Delft3D

Model validation was performed by comparing the modelled results with available measured data. First, the proper astronomical components were chosen through a sensitivity analysis. Use as input of the astronomical components of the Ancona tide well reproduces the astronomical sea level variation at the Misa River Mouth, where the modelled data were compared with the data recorded by the tide gauge of the MORSE project (described in section 2.1). Comparison of the modelled wave climate and timeseries recorded by the offshore MORSE ADCP (described in section 2.1) reveals that the WAVE module correctly propagates the waves from the deep waters to the shore. The results of such validations are reported in Figure 5.

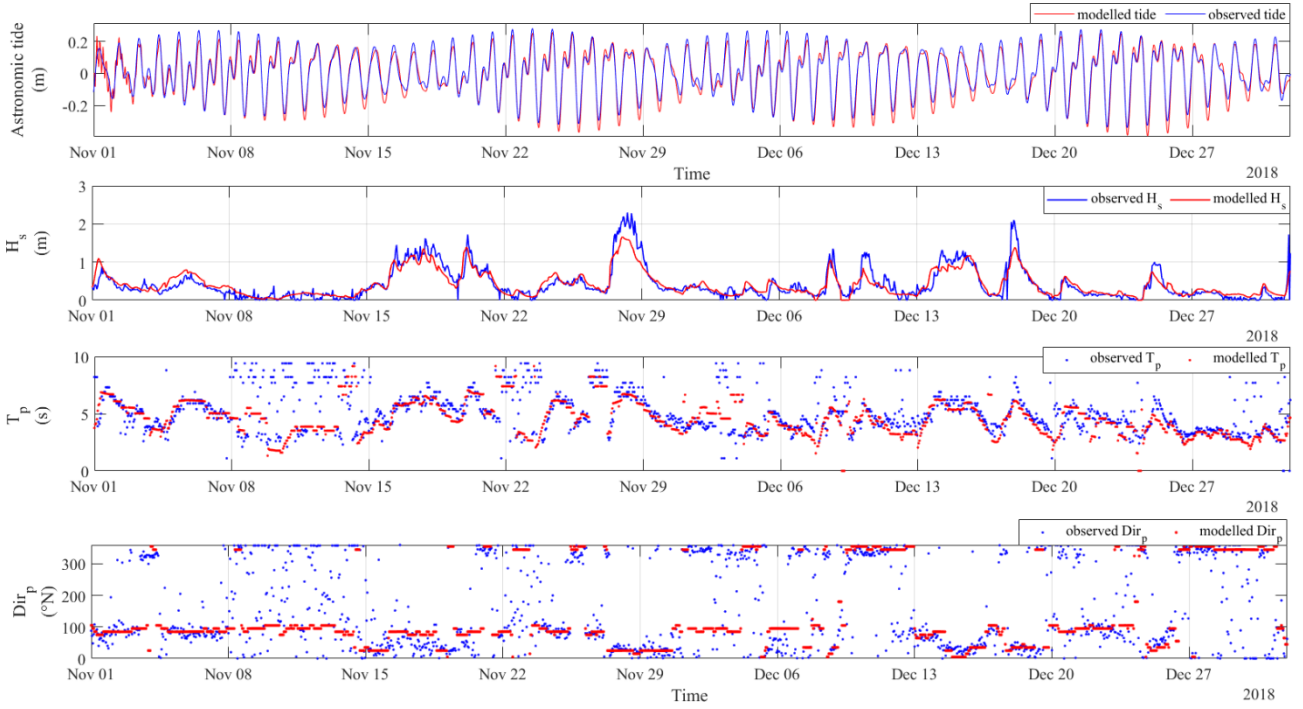


Fig. 5. Top panel: comparison between the modelled (red) and observed (blue) astronomic tide for November-December 2018. Second, third and fourth panels: comparison between modelled (red) and observed (blue) wave significant height, peak period and peak direction for November-December 2018.

One further validation of the model performances was done by comparing the modelled velocity with the velocity measured during the EsCoSed project, carried out in 2014, at QR2 and QR3 (see [Brocchini et al., 2017](#)). The WAVE module was forced using Copernicus CMEMS timeseries of wave climate, while the FLOW module was forced using the astronomical components of the Ancona tide at the offshore boundary, zero-gradient Neumann water level conditions at the cross-shore boundaries and a discharge timeseries at the “river section”. We first computed the discharge timeseries from the river water level data measured at “Bettollele” using the available rating curve. Then, since the Bettollele station is 10 km upriver of the “river section” of our interest, where the discharge timeseries is imposed, we used the HEC-RAS package to obtain the discharge timeseries at such section. Furthermore, we associated an error to the discharge timeseries due to the uncertainty in the rating curves. Such error was obtained by comparing the discharges computed through the rating curve with the available measured discharges provided by the Civil Protection. We found a mean error of 26.83% and we calculated two discharge timeseries, namely “inf” and “sup”, by, respectively, subtracting and adding the error to the original discharge timeseries. We run three simulations: with 1) the original timeseries, 2) the “inf” timeseries and 3) the “sup” timeseries to obtain the associated velocity timeseries. The velocity timeseries obtained using the original discharge timeseries (v_{mod}) at QR2 and QR3 is shown in Figure 6 (blue line). The band of velocity obtained with both the “inf” and “sup” timeseries (blue band in Figure 6) was taken as the area where the measured velocities had to fall to satisfy the validation.

While the velocity provided by the simulations (v_{mod}) is averaged over the total water depth, that made available by the EsCoSed dataset was averaged from the riverbed to 1.3 m above the riverbed. Thus, we could not directly compare the modelled velocity with the measured one, but some extra elaborations were needed. First, we projected the measured velocities in the river current direction ($v_{obs,1.3}$, red line in Figure 6); then, we used such data and the surface velocities measured by the EsCoSed drifters (see [Brocchini et al., 2017](#)) to extrapolate some vertical velocity profiles at QR2 and QR3. We could extrapolate three and two profiles for QR2 and QR3,

respectively. It was not possible to extrapolate profiles when the surface velocity was not available. Then, we computed the mean velocity over the total water depth for each profile ($v_{\text{obs,drift}}$, red diamonds in Figure 6) and the difference between such value and $v_{\text{obs,1.3}}$. Finally, we averaged the differences, obtaining 0.13 m/s and 0.11 m/s for QR2 and QR3, respectively. We added such values to $v_{\text{obs,1.3}}$ to obtain a datum (v_{obs} , red dashed line in Figure 6) more suitable for the comparison with the modelled depth-averaged velocity. The result of the validation is represented in Figure 6.

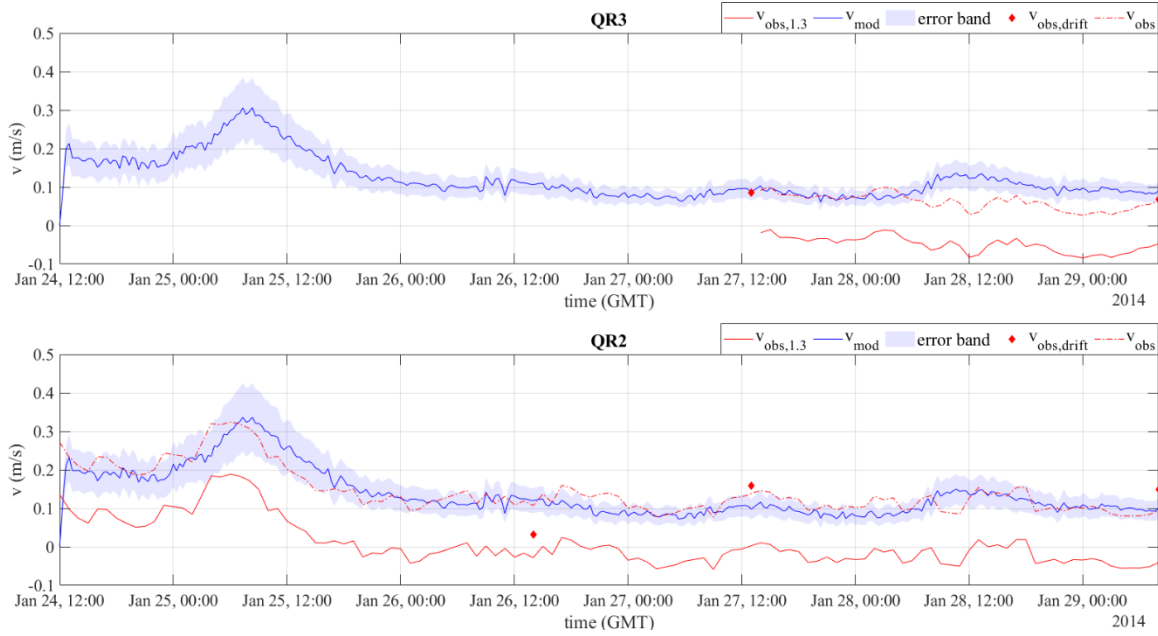


Fig. 6. Validation of the model performances.

3. Results

3.1. Field observations

We here provide a very short summary of all field observations, which are clustered in the following as function of four main processes. The evolution of the area and centre of mass of the emerged bar, detected by the images, was correlated with the river and nearshore forcing acting on the estuary. We analysed the images available from 2016 to 2019; however, except for several days in April 2016, the bar was not regularly emerged until 2017. Therefore, the data until 2017 have not been discussed here. For each year, a global view of the timeseries of significant wave height, H_s , and direction, river discharge, river and sea water levels, astronomic tide, area of the bar, and x and y coordinates of the bar centre of mass, is reported (Figures 8, 9, 10). In the first panel of such graphs, waves coming from NNE and from E, are highlighted in blue and red, respectively. They represent the most frequent waves approaching the coast of Senigallia (see Figure 7). Moreover, waves from NNE are those directed perpendicularly to the estuary. The bottom panels of Figures 8, 9 and 10 refer to the rotated reference system (Figure 2b), where an increase of the x and y coordinates gives a displacement of the bar centre of mass toward the east riverbank and upriver, respectively. Moreover, some typical behaviours were highlighted: rapid downriver migrations due to river discharge were denoted by green arrows (labelled D1-D4), rapid upriver migrations due to waves by orange arrows (labelled W1-W4) and slow upriver migrations due to waves and in the absence of river discharge by dashed red boxes

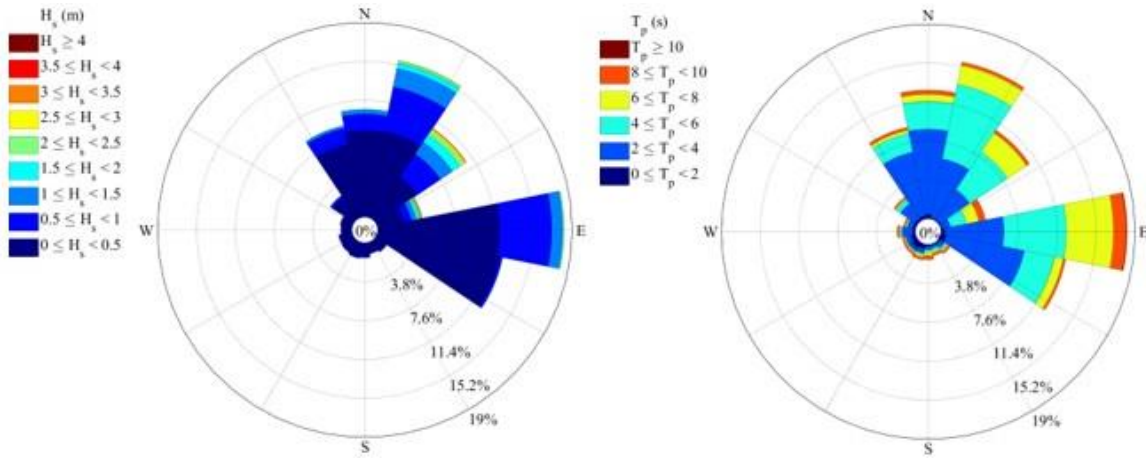


Fig. 7. Wave roses.

(labelled P1-P5). Periods of time when observations from the SGS station were unavailable are highlighted in yellow in Figures 8, 9 and 10. To improve readability, graphs were divided into two parts, i.e. January-June and July-December.

The bar mainly formed along the final 180 m stretch of the river, on the west bank, due to the mechanisms that govern downriver and upriver sediment transport. In fact, the interested stretch of the river is located along the inner bank of a mild river bend, where the downriver sediment transport, forced by the river discharge, finds a depositional area due to centrifugal actions. Moreover, waves force a local net alongshore sediment transport directed, in the mean, toward the NW, bringing some extra sediment in the bar area. Thus, in the final stretch of the river, some convergence occurs of river and sea driven sediment fluxes. This, added to the already rising riverbed level due to reduced precipitation and absence of flood discharge (see Figure 16), leads to the formation and emergence of the observed bar.

The correlation of the observed data with the estuarine forcing shows that the main factors driving the evolution of the bar are the river discharge and the waves. The sea water level plays also a role in determining the emerged portion of the bar. Moreover, in 2019, a more complex system of bars appeared that allowed us to inspect the effects of the various forcing factors. These and related dynamics are illustrated in the following sub sections.



Fig. 8. Time series of wave height and direction ($^{\circ}\text{N}$) (top panel), river discharge (second panel), river and sea water levels (third panel), area of the bar (fourth panel), and bar centre of mass (fifth panel) are shown for 2017 from (a) January-June and (b) July-December. In the top panel, wave directions within 5°N and 35°N represent waves perpendicular to the channel. Periods of time when observations from the SGS station were unavailable are highlighted in yellow. Dashed red boxes bound the periods reported in Figure 12. Green arrows identify the events D1, D2 and D3; orange arrows identify the events W1, W2 and W3.

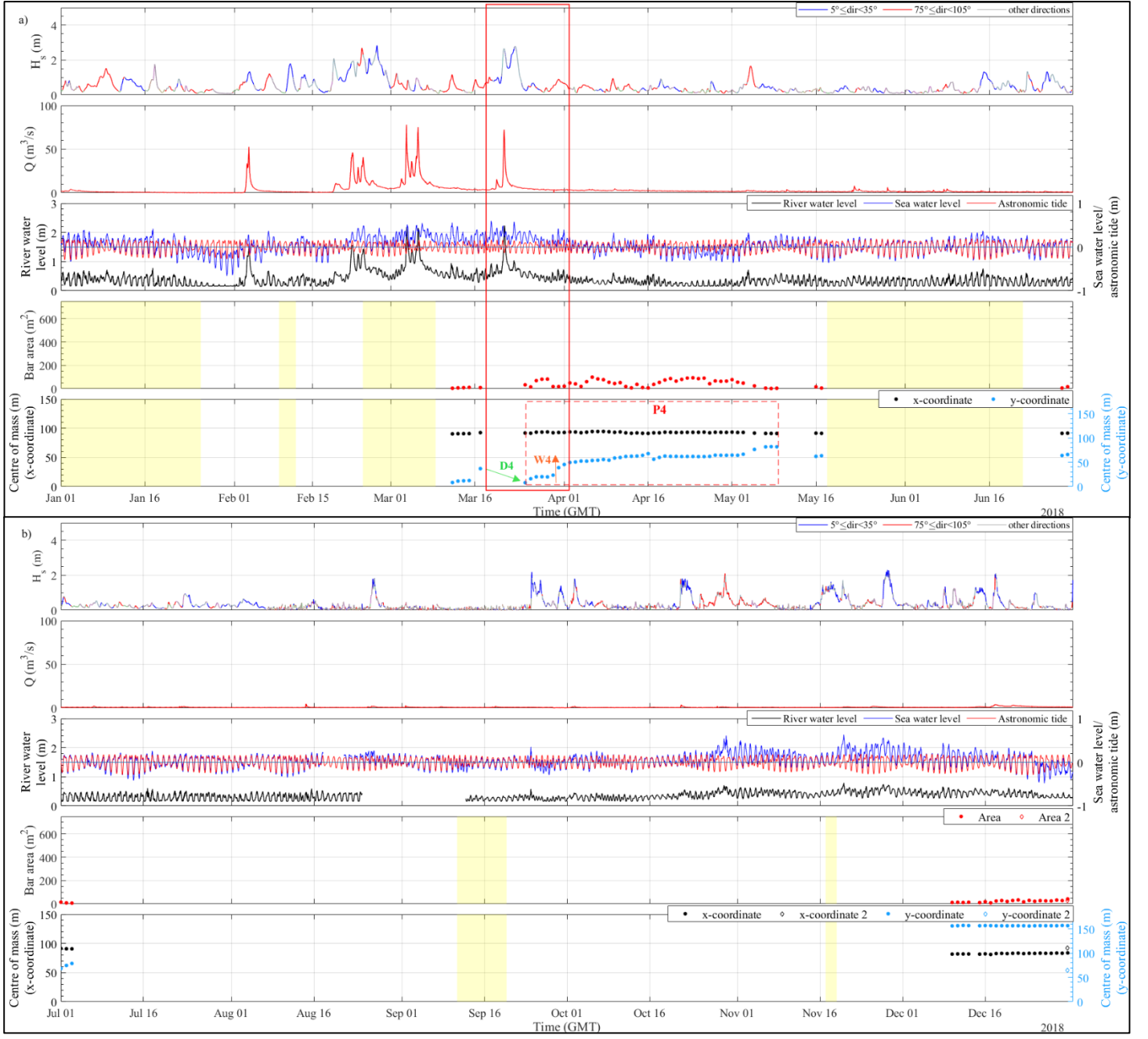


Fig. 9. Time series of wave height and direction (top panel), river discharge (second panel), river and sea water levels (third panel), area of the bar (fourth panel), and bar centre of mass (fifth panel) are shown for 2018 from (a) January-June and (b) July-December. In the top panel, wave directions within 5°N and 35°N represent waves perpendicular to the channel. Periods of time when observations from the SGS station were unavailable are highlighted in yellow. Dashed red boxes bound the period reported in Figure 12. The green arrow identifies the event named D4; the orange arrow identifies the event named W4.

1
2
3
4
5

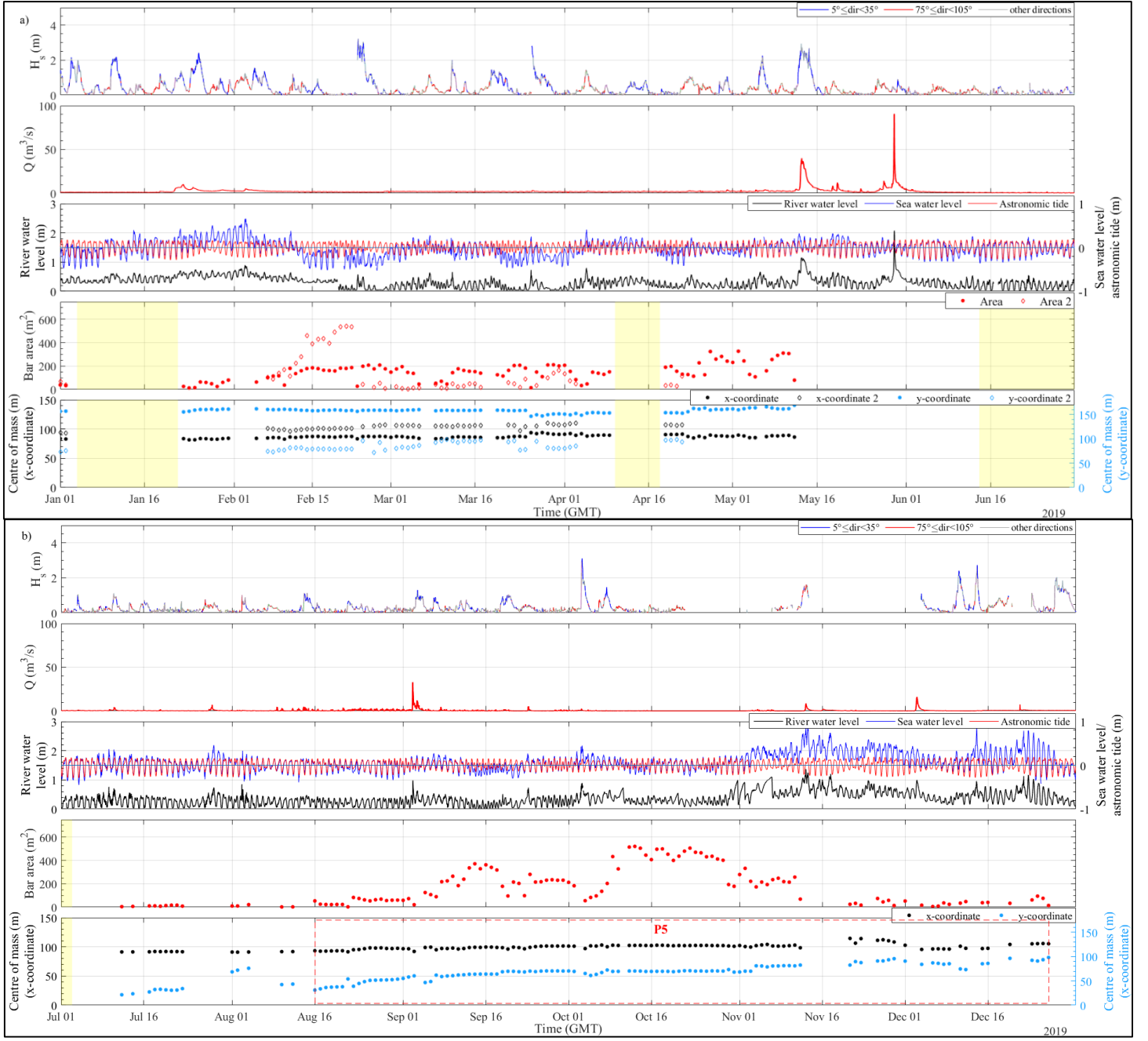


Fig. 10. Time series of wave height and direction (top panel), river discharge (second panel), river and sea water levels (third panel), area of the bar (fourth panel), and bar centre of mass (fifth panel) are shown for 2019 from (a) January-June and (b) July-December. In the top panel, wave directions within 5°N and 35°N represent waves perpendicular to the channel. Periods of time when observations from the SGS station were unavailable are highlighted in yellow. Dashed red box bounds the time period reported in Figure 12 (P5).

1 The river discharge forcing

2 Observations suggest that the action of the river played a fundamental role in the downriver migration of the bar. In fact, Figure 8a
3 shows four significant peaks in the discharge and river water level time series, after which the bar resurfaced downriver from where it
4 was detected previously. These events took place on 18 January, 6 February, 25 February and 7 March 2017, hereinafter named D1,
5 D2 and D3, the third and fourth peaks being treated as a single event (D3) because the bar did not resurface between the peaks. These
6 events also highlighted the role of other two factors that contributed to determine the extent of the displacement of the bar: the
7 simultaneous action of the waves and the position of the bar along the channel before the occurrence of the river discharge. The first
8 and the second events were characterized by a similar discharge and downriver bar position along the channel, respectively $20.9 \text{ m}^3/\text{s}$

and 78.7 m for D1 and 36.7 m³/s and 81.4 m for D2. However, the displacement of the bar was smaller for the first event than for the second one ($\Delta_{D1}=20 \text{ m} < \Delta_{D2}=43.4 \text{ m}$, where $\Delta_{Di} = y_{i,end} - y_{i,start}$ with $i=1,2,3$). This was due to the waves acting simultaneously with the river discharge, which were higher during the first event (H_s reaching 3.6 m) than during the second event ($H_s = 2.1 \text{ m}$). Comparing the second and third events, they were characterized by similar wave heights (2.1 m). Since D3 was characterized by a maximum river discharge that was more than twice the discharge of D2, one could have expected a larger bar displacement for D3. However, this did not occur ($\Delta_{D2}=43.4 \text{ m} \cong \Delta_{D3}=42.7 \text{ m}$) because of the bar position, which was 81.5 m for D2 and 46.6 m for D3. Thus, the bar of the second event was located about 35 m more upriver than the bar of the third event, this exposing it more intensely to the action of the river. And, on the contrary, the bar of the third event was more intensively exposed to the action of the waves.

The role of both the simultaneous wave action and the bar location is confirmed by the event of 21 March 2018 (Figure 9a), where a discharge of 72.3 m³/s, i.e. similar to that of the third event, produced a 29 m downriver migration of the bar, initially located at 36.8 m along the y-axis of the channel. The concurrent wave action ($H_s=2.6 \text{ m}$) and position of the bar, located quite downriver, reduced the effect of the river discharge on the bar displacement.

Figure 11 shows the final stretch of the river, with the jetties coloured in grey and the dashed black line indicating the area not visible by the cameras. The reference system of this graph is the same as Figure 2b. The four panels illustrate the position and shape of the emerged part of the bar before (blue) and after (red) the occurrence of the river discharge for events D1, D2, D3 and D4. They clearly show that the bar reappeared downriver after the discharge peaks, the displacement also highlighted by black arrows.

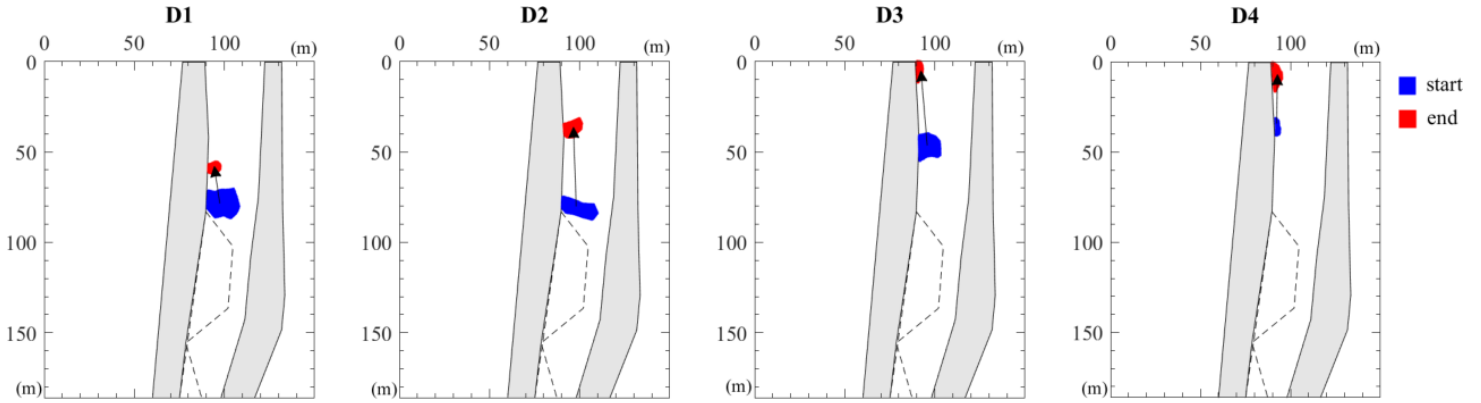


Fig. 11. Positions and shapes of the bar before and after the discharge peaks occurred in events D1, D2, D3 and D4. Black arrows indicate the downriver migrations of the bar.

The wave forcing

The action of the waves, as opposed to that of the river current, caused a gradual upriver migration of the bar during the periods when the river discharge was very low. In particular, the y-coordinate of the bar centre of mass showed a gradual increase within periods P1, P2, P3, P4 and P5 (Figures 8a, 9a and 10b), this meaning that the bar slowly migrated upriver. This is also clearly visible in Figure 12, where the final stretch of the river is represented like in Figure 11, but with the positions of the bar centre of mass during P1, P2, P3, P4 and P5 reported with different colours as function of the day they occurred. Upriver migrations are highlighted by black arrows. Moreover, waves caused impulsive displacements of the bar that determined a “staircase behaviour” of the y-coordinate of the centre of mass together with a decrease of the bar area. This occurred, for example, on 25 January, 27 March and 2 April 2017 (Figure 8a)

1 and on 31 March 2018 (Figure 9a), hereinafter named W1, W2, W3 and W4. The first three cases were characterized by significant
2 wave heights of about 1 m, but different wave directions. While the waves of W1 and W2 were directed perpendicularly to the estuary
3 ($5^\circ\text{N} \leq \text{dir} < 35^\circ\text{N}$), the W3 waves came more from the east ($75^\circ\text{N} \leq \text{dir} < 105^\circ\text{N}$). The displacements were all of order 10 m and took
4 place in one day. However, little differences between the cases could be found, since $\Delta_{W1} > \Delta_{W2} > \Delta_{W3}$ ($\Delta_{Wi} = y_{i,\text{end}} - y_{i,\text{start}}$ with
5 $i=1,2,3,4$). Starting from W1 and W2, they were characterized by bar areas and downriver bar locations of about 150 m² and 58.8 m
6 and 190 m² and 33.4 m, respectively. Despite the bar of event W2 was located more downriver, i.e. was more exposed to the wave
7 action, its area was larger than that of W1 and, consequently, its displacement was smaller. Thus, the influence of the bar area was
8 more effective than that of the bar location. In cases with same bar areas, like W2 and W3, both the position of the bar and the direction
9 of the incoming waves played a role. In fact, the W2 bar moved farther because of both the waves coming perpendicularly to the estuary
10 and its position, about 16 m downriver with respect to the bar of W3. Differently from the events dominated by the river action, the

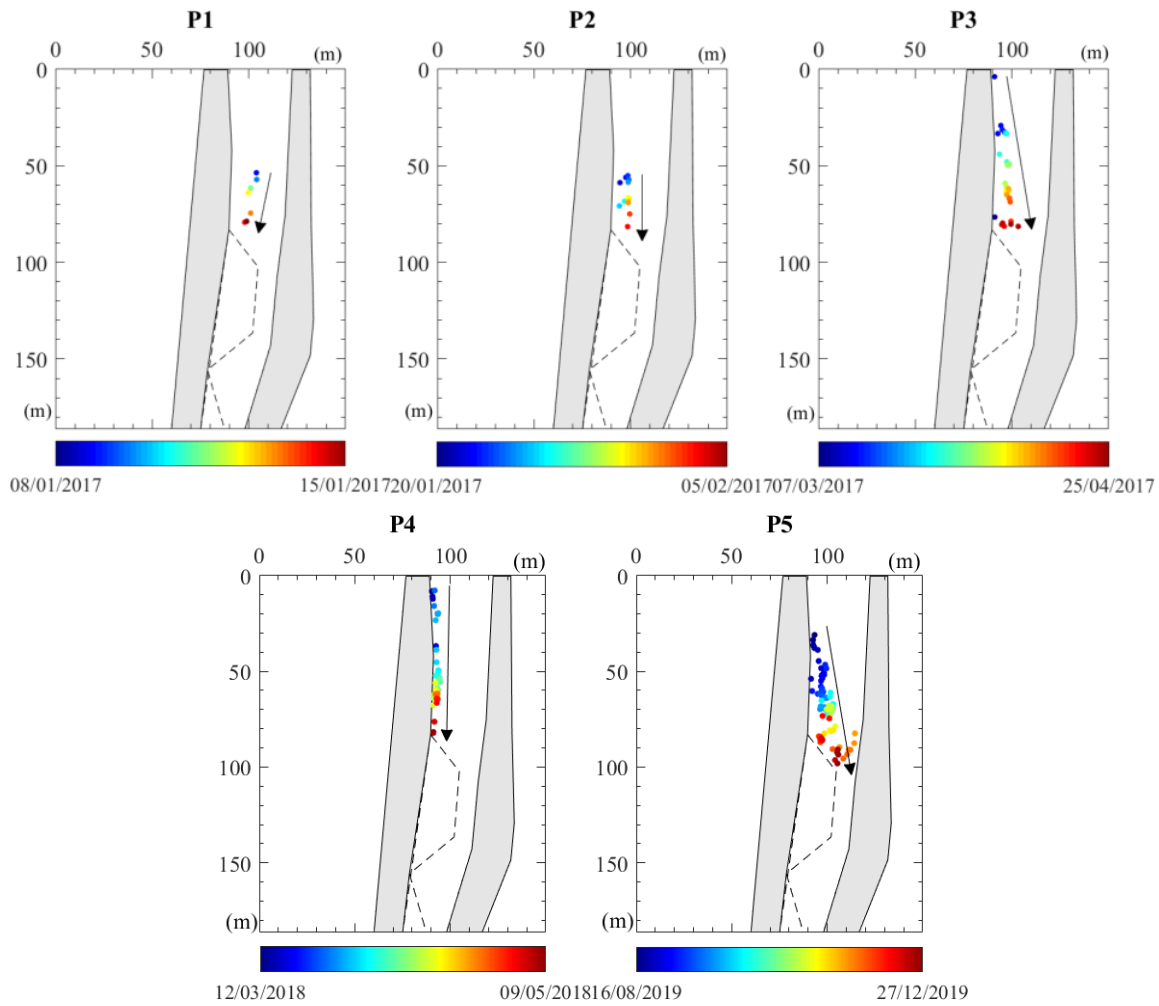


Fig. 12. Positions of the bar centre of mass, within the periods highlighted in Figures 8a, 9a and 10b, coloured depending on the day they occurred (see colorbar). Black arrows indicate the upriver migration of the bar within each period.

11 cases dominated by waves seem to be less sensitive to these factors, being the difference of the displacements fairly small ($\Delta_{W1} -$
12 $\Delta_{W3} = 3$ m) with respect to that caused by the river discharge ($\Delta_{D2} - \Delta_{D1} = 23.4$ m). The displacement of W4 was larger ($\Delta_{W4} = 26.1$
13 m), but it took 3 days to evolve. The wave forcing was mild ($H_{s,\text{max}} = 0.84$ m) and came from the east ($75^\circ\text{N} \leq \text{dir} < 105^\circ\text{N}$), but it was

enough to cause some bar upriver migration. This was probably due to the very small area of the bar (about 20 m²) and its closeness to the mouth (26 m).

A system of two bars

On 31 December 2018, a second sediment mound started emerging at about 55 m (downriver of the previously emerged bar). The second bar is represented by empty diamonds in the last two panels of Figure 9b. Continuing into the first part of 2019, two emerged deposits were visible with one located in the area framed by cameras C1 and C2 and the other located in the area framed by cameras C3 and C4 (see Figure 2b and Figure 13). The two emerged deposits were part of the same large underwater shoal that emerged with a complex shape; however, the area of the river between these two deposits was not visible because of the limited field of view of the cameras. We decided not to extrapolate the hidden area, but to leave the two bars separated. Therefore, Figure 10a shows two different timeseries for the area and the centre of mass of the bar where full circles represent the main bar and empty diamonds represent the second emerged deposit.

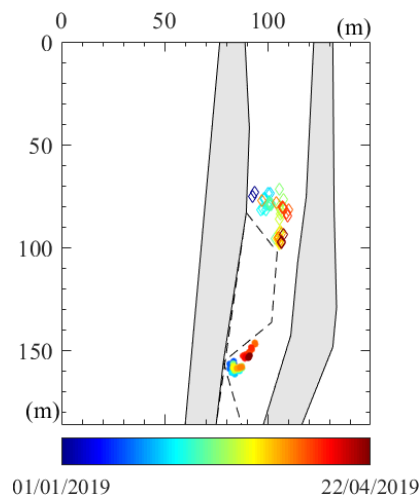


Fig. 13. Positions of the bars centre of mass within the period of coexistence of two bars, coloured depending on the day they occurred (see colorbar). Empty diamonds and full circles represent the most downriver and the most upriver bar, respectively.

Although this configuration made the analysis more complicated, some of the abovementioned mechanisms for the evolution of the bar could be recognized. The effect of the waves could be seen in the event occurred on 23 February 2019, characterized by significant wave height of about 3.2 m coming from NNE. Before the storm, the area of the most downriver bar (red diamonds in the fourth panel of Figure 10a) had reached values of 534 m², also due to a maintenance operation carried out on 19 February 2019 to flatten the bar. The waves, directed perpendicularly to the estuary, submerged the bar, already lowered by the maintenance operation, and caused an abrupt decrease of the bar area. In addition, the storm mobilized sediments and remodelled the bar, which reappeared with an irregular shape in the following days. Such irregular shape caused the oscillation of the centre of mass, thus in this case it was not possible to observe the upriver displacement of the bar due to the wave action. A decrease in the bar area occurred also for the most upriver bar (red circles in Figure 10a), whose centre of mass remained stable. Being the most upriver bar located very upstream, at about y=160 m, and sheltered by the most downstream bar, the waves affected only its area, lowering it because of an increase of the local water level. Similar reductions of the area or submersions of the most upriver bar verified on 7-8 March, 18-19 March, 26 March and 4 April 2019, even under milder waves ($1.2 < H_s < 2.8$) coming mainly from NNE and E. Being the area of the most downriver bar greatly reduced after the event of 23 February, its sheltering of the most upriver bar decreased, allowing also the milder waves to affect the

emerged area of the upriver bar. The centre of mass of the upriver bar did not show significant migrations because the bar was located too upstream to be moved by the storms.

There were no discharges during the period of coexistence of the two bars, so the effect of the river current on this complex system could not be observed. However, two significant river discharges occurred on 13 and 29 May 2019, when only the most upriver bar was emerged, which caused the transport of the sediment toward the sea and, consequently, the bar reappeared about 150 m downriver in July (Figure 10b). Despite the fact that the discharge of 13 May 2019 was associated with a storm event (H_s of about 3 m), here the waves could not play a fundamental role because the bar was located very upriver in May 2019 ($y = 169$ m). After 13 May, the wave climate was very mild and characterized by highly variable directions, this reducing the effect of the waves and allowing the predominance of the river flow on the behaviour of the bar.

Water level induced modulation

The overall increase or decrease of the sea water level affected the emerged area of the bar, lowering or increasing it, respectively. For example, in November 2019 (Figure 10b), the sea water level was permanently above the mean water level, this probably contributing to the reduction of the bar emerged area from 500 m² to 26 m². In contrast, during February 2019 (Figure 10a), the sea water level decreased from about 0.2 m to about -0.5 m and the emerged area of the bar significantly increased from 41 m² to 534 m².

3.2. Numerical simulations

Parametric simulations

The results of the parametric simulations, run to highlight the role of the various forcing, are illustrated in Figure 14, which reports the section along the left riverbank extracted from the bathymetry using the reference system of Figure 2b. The top panel shows the evolution of the riverbed for the simulations with input peak discharge equal to $Q=50\text{m}^3/\text{s}$ and $Q=100\text{m}^3/\text{s}$, with and without tide. The chosen discharge values are comparable to the 1-year return period discharge. The river discharges eroded the riverbed both in the upper channel and bar location, while deposition occurred just out of the river mouth. The highest discharge eroded about 9 cm along the river (6 more cm than the lowest discharge) and a maximum of 37 cm on the bar (27 more cm than the lowest discharge), this suggesting an erosion directly proportional to the discharge intensity. In particular, doubling the discharge led to an erosion about four times larger. The comparison with the simulations run without tide shows that the tide did not considerably influence the behaviour of the bar, but only caused some differences on the final bed level. Along the considered section, on average, the differences between the final bed level with and without tide were of 4.2 mm and 1.6 cm for the simulations with 50 m³/s and 100 m³/s, respectively. The numerical results reinforced the observations. Although we could not directly compare such results with the discharge events D1-D4 because of the different bathymetries and durations - the real-life cases being characterized by an emerged bar over around five days while the modelled one characterized by a large submerged deposit over a period of two days - we still recognized the same behaviour. In fact, the D1-D4 observed events showed the submersion of the bar due to the river discharge, this suggesting bar erosion, also predicted by the simulations. The computed downriver bar migration, made dimensionless through the river width, was in the order of

4 river widths, while due to the differences of the observed scenario, the field displacements (Δ_{D1} , Δ_{D2} , Δ_{D3} , Δ_{D4}) were all smaller than 2 river widths.

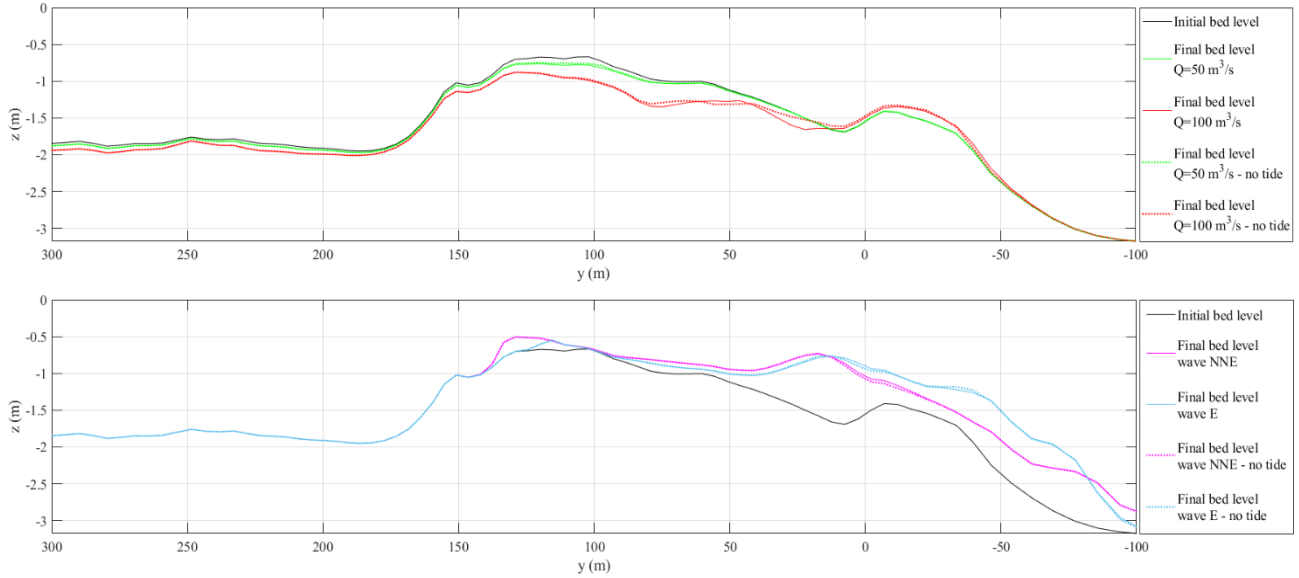


Fig. 14. Results of the parametric simulations. The top panel shows the evolution of the bed for the river discharge only simulations: the black solid line represents the initial bed level; the green and red lines represent the final bed level for the simulations with $Q=50 \text{ m}^3/\text{s}$ and $Q=100 \text{ m}^3/\text{s}$, respectively; the solid and dotted lines refer to the case with and without tide, respectively. The bottom panel shows the evolution of the bed for the wave only simulations: the black solid line represents the initial bed level; the magenta and blue lines represent the final bed level for the simulations with NNE waves and E waves, respectively; the solid and dotted lines refer to the case with and without tide, respectively. The reported section is along the left riverbank, so the x-axis corresponds to the y-axis of Figure 2b that origins from the river mouth and is positive upriver. The bed level (z) is zero at the water surface and negative downward.

The bottom panel of Figure 14 shows the riverbed evolution for the simulations run with both NNE and E waves, with and without tide. Such waves were estimated in relation to the 10-years return period local waves (H_s of the order of 4 m) also observed during the period of our interest. The waves brought sediments inside the river mouth, causing the crest of the most seaward bar to grow and move upriver. In particular, waves coming from NNE caused a crest accretion of about 70 cm and a displacement of about one river width, while waves coming from E caused a crest accretion of about 65 cm and a displacement smaller than one river width. Moreover, waves from NNE produced a 20 cm deposition and a displacement smaller than one river width also of the portion of the bar located about 120 m upriver from the river mouth, while the E waves only caused its accretion of 13 cm (negligible migration). This confirming that the northeasterly waves, entering perpendicularly to the estuary, had a stronger effect on the bar than the easterly waves. In fact, they could modify the bar not only at the river mouth, but also in its upriver part. Both waves did not affect the inner slope of the bar and the upriver evolution. Again, the tide did not influence the behaviour of the bar. The above analyses reveals that the 10-years return period NNE waves induce: 1) a much smaller evolution of the most upriver bar than the 1-year return period discharge; 2) slightly larger vertical excursions and much smaller migrations of the most seaward bar than the 1-year return period discharge. This clarifying the dominance of the sediment expulsion out of the river mouth by the river discharge than the upriver transport by the waves.

1 Real-life simulation

2 The event highlighted by the red box in Figure 9a was reproduced with Delft3D to critically compare the results of the numerical
 3 simulations with the observed data. The event was characterized by a complex combination of forcing, which first led to a downriver
 4 bar migration, then followed by an upriver migration. On 21-23 March 2018, a storm occurred, with two wave height peaks of about
 5 2.6 m and 2.8 m, respectively, on 21 and 23 March 2018. On 21 March a peak in river water level also occurred. The river discharge
 6 was computed by using the rating curve of “Bettollele”, validated until 5 March 2018, and by transporting it to the river section of the
 7 model using HEC-RAS. The imposed discharge reached about 72 m³/s. The observed data showed: (1) the presence of an emerged bar
 8 along the west riverbank (y-coordinate about 37 m) on 17 March 2018, before the storm and discharge; (2) the submersion of the bar
 9 during the storm due to the increase of the water level; (3) the emergence of the bar on 25 March (y-coordinate about 8 m), after the
 10 storm and discharge events, highlighting a downriver migration of around 29 m; (4) the upriver migration of the bar with the y
 11 coordinate increasing from about 8 m to about 45 m (1 April), while the x coordinate remained around 91 m, suggesting that the bar
 12 remained anchored to the west riverbank. Based on the observations, we expected to see both the effect of the river flow and the waves.
 13 In particular, since the peaks in discharge and wave height occurred on the same day and were followed by a second wave height peak
 14 two days later, we expected that the river would not have caused a significant downriver sediment transport (as we saw, for example,
 15 in 2017). However, we would still await for some riverbed erosion due to the river discharge. On the other hand, we expected to see
 16 upriver sediment transport, due to storm waves, since the field observations showed an upriver migration of the bar. Figure 15 shows
 17 the forcing of the event in the first two panels and the evolution of the observed x and y-coordinates of the bar centre of mass in the
 18 third panel. The fourth and fifth panels show the evolution of the modelled bed level along the longitudinal section adjacent to the west
 19 riverbank, where the bar is located. The arrows in the fourth and fifth panels highlight the effect of the discharge and of the waves,
 20 respectively. The black curve in the fourth panel represents the initial bed level (18 March 2018), characterized by two main crests.

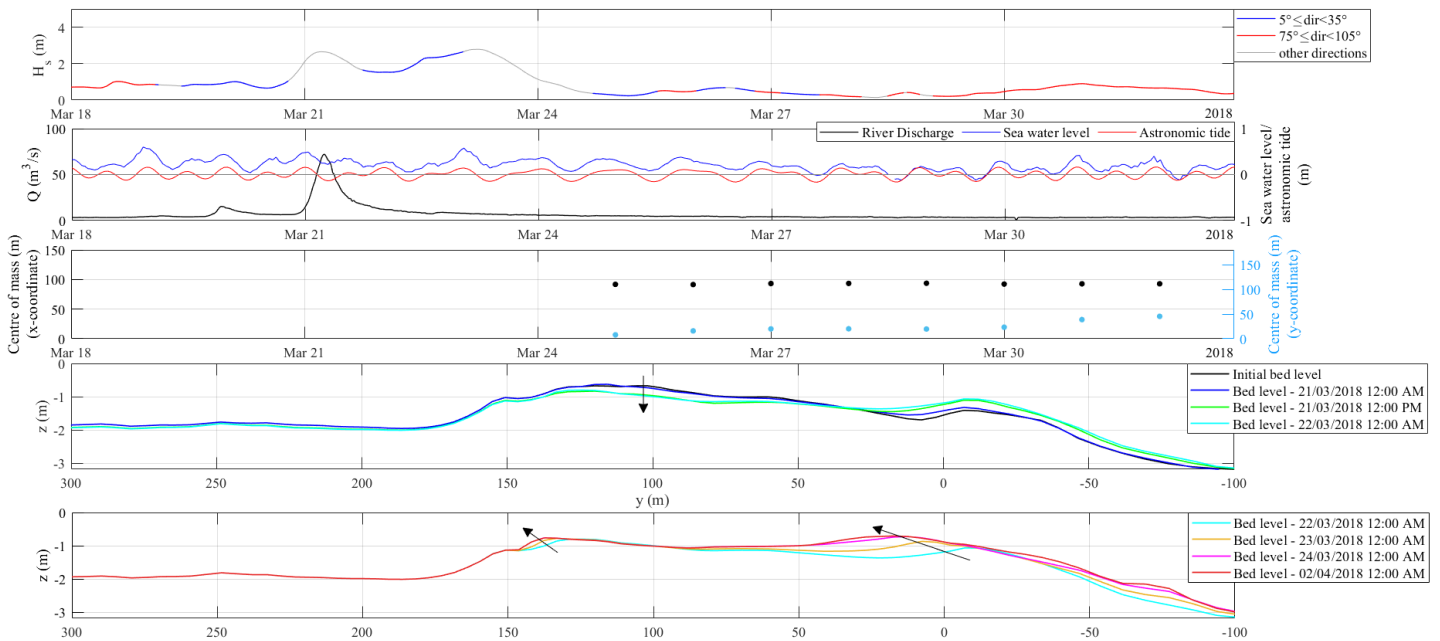


Fig. 15. Simulation of the real-life event: the top panel reports the wave significant height and direction; the second panel reports the river discharge, the sea water level and the astronomical tide; the third panel reports the observed x and y-coordinates of the bar centre of mass; the fourth and fifth panel shows the riverbed evolution along the longitudinal section adjacent to the left riverbank. The section was reported to the local reference system (Fig. 2b). The bed level represents the distance from the mean water level to the riverbed, negative downward. The evolution of the riverbed was divided into two panels to better highlight the effects of the river discharge and of the waves.

The cyan line identifies the bed level after both the peaks in discharge and wave height; an accumulation (about 35 cm) of sediment occurred at the location of the most seaward crest, while the other crest, more directly exposed to the river flow, was eroded (max 31 cm, indicated by the black arrow). Moreover, the riverbed upstream of the bar was also slightly eroded (about 8 cm). As expected, some significant erosion of the bar occurred as due to the river discharge. Then, the storm occurred on 23 March 2018 pushed the sediments inside the river mouth and caused an increase in height of the outer crest. The orange and magenta lines describe the evolution of the bed until the end of the second wave height peak. They clearly show the accretion and upriver translation of the crests (indicated by the black arrows). The simulations confirmed that waves were responsible for some upriver sediment transport and migration of the deposit. The most evident displacement and accumulation occurred for the most seaward bar crest, that translated some 24.4 m upstream and increased in height by about 36 cm. After the storm, there was a very slight modification of the most seaward crest due to the easterly waves of 31 March 2018.

4. Discussion

The results of the analysis on the migration of the bar formed inside the MR estuary show the complexity of the interaction between the different forcing that govern the morphodynamics of the environment. Overall, the bar emerges inside the river mouth (inner bar) and it is almost always adjacent to the west riverbank. The location where the bar forms suggests a decrease of the river flow velocity inside the final reach of the MR and some contribution of the wave-driven flux. Moreover, bathymetric surveys showed a growing elevation of the riverbed in the final reach, as visible in Figure 16, likely due to the reduced amount of precipitation and river discharge occurring over the last years. In the past, the morphodynamics of the MR mouth was characterized by a typical cyclic behaviour with sediment deposition under weak river flow (summer conditions) and sediment erosion toward the sea under an intense river water jet (winter conditions), as highlighted during the field experiments performed in 2013 and 2014 (Brocchini et al. 2017). However, over the last few years the deposition inside the river highly exceeded the erosion, leading to the emersion of a more stable deposit since 2017. Figure 16 shows the bed level variation from 2013 to 2020 and highlights the increase of the riverbed level mostly in the area where the bar forms. The second panel of Figure 16 displays a situation similar to Figure 8d of Brocchini et al. (2017), which describes the wintertime condition between September 2013 and February 2014. The highest deposition occurred in the final reach of the river and beyond the channel, to the north, while erosion occurred just beyond the south pier. However, considering that from April 2018 through October 2018 (when the bathymetric survey was performed) no discharge events occurred, we did not observe significant erosions in the upriver stretch of the channel, as was observed by Brocchini et al. (2017). The third panel of Figure 16 represents the bed variation between September-October 2018 and March 2020. During that period, the absence of precipitations and river discharges caused an accumulation of sediment within the whole channel and mostly in the location where the bar emerged. Moreover, just outside the river mouth the pattern reversed, with erosion and deposition occurring to the north and seaward of the south pier, respectively. A

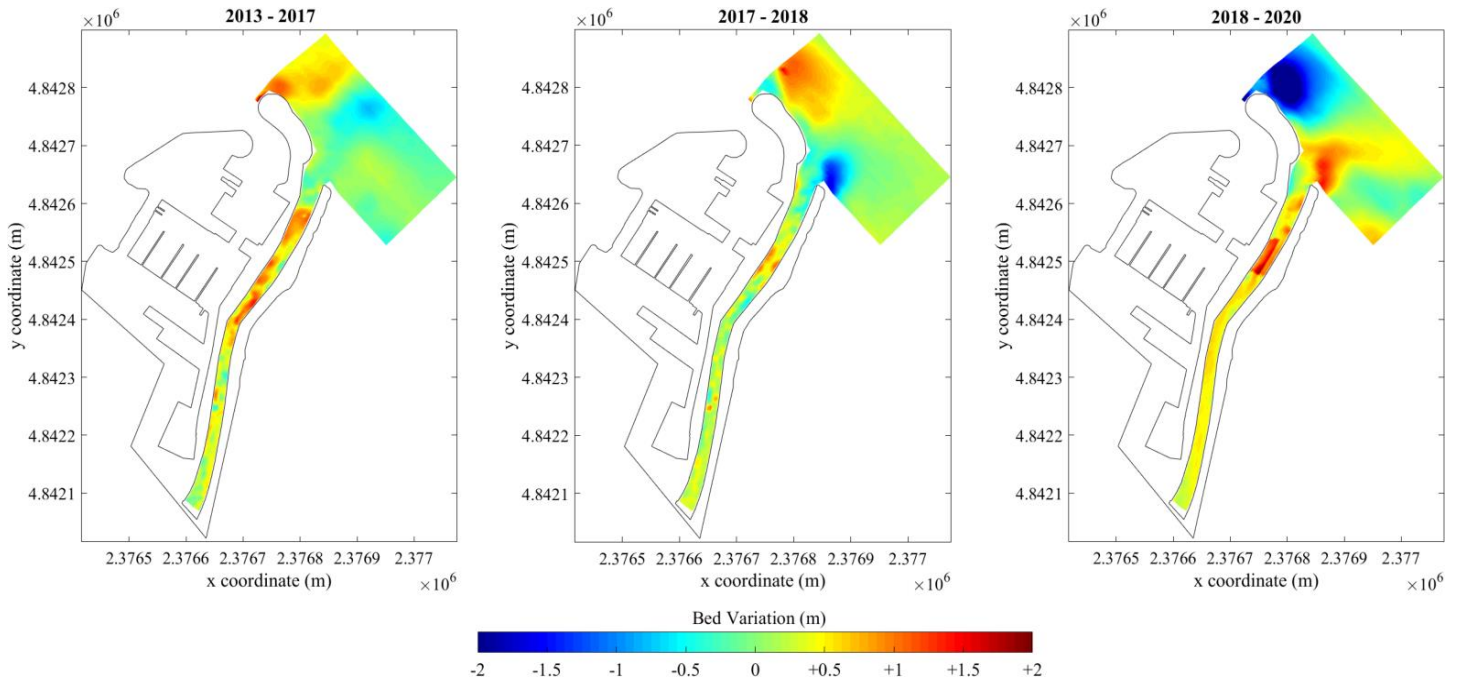


Fig. 16. Variation of the riverbed from 2013 to 2020.

1 similar situation occurred in summertime conditions, as shown in Figure 8c of [Brocchini et al. \(2017\)](#). Usually, the large shoal present
2 in the **final** reach of the river emerged in a single location generating a single bar, but sometimes it emerged in different areas generating
3 complex morphological shapes, as happened in February or September 2019.

4 Our observations (Figure 8a, Figure 11) show that the bar migrated downriver when the estuary dynamics were dominated by the action
5 of the river discharge. The relationship between river forcing and downriver migration was exemplified in the first part of 2017, when
6 four increasing peaks in river water level and discharge caused downriver migrations of the bar. Although the wave climate, in the
7 same days, was not weak, with significant wave heights larger than 3 m for the first two events, the action of the river prevailed and
8 caused a downriver migration of the bar. For example, the event that caused the maximum downriver migration of the bar occurred on
9 6 February 2017, producing a change of the y-coordinate of the bar centre of mass from about 81.4 m on 5 February to about 38 m on
10 11 February. The longitudinal displacement of the centre of mass was of about 1.74 river widths. Downriver migrations were also
11 observed when the bar was submerged (February-March 2018, May 2019) as due to a few isolated river discharge events. These river
12 discharges caused a clear seaward sediment transport. In fact, after such events, the bar emerged again farther downstream from where
13 it had disappeared. For example, the bar disappeared on 12 May 2019 at $y=169$ m and reappeared on 12 July 2019 at $y=21$ m, about
14 148 m downriver. The seaward sediment transport and consequent downriver migration of the bar always and only correlated with
15 river discharge peaks, the upriver flow acceleration mobilizing the sediments and leading to erosion of the bar top and upstream face,
16 the lee-side flow deceleration leading to sediment deposition ([Edmonds and Slingerland, 2007](#)). The parametric simulations forced
17 using two different river discharges of $50 \text{ m}^3/\text{s}$ and $100 \text{ m}^3/\text{s}$, comparable in size to the 1-year return period discharges, showed that the
18 whole riverbed was eroded, with maximum erosion occurring at the most upriver bar crest (top panel of Figure 14), and downriver
19 migration in the order of four river widths. Moreover, they showed sediment accumulation just downstream of such bar crest, suggesting
20 the occurrence of downriver sediment transport due to the river forcing. These simulations also demonstrated that the amount of erosion
21 and consequent deposition is directly proportional to the river discharge, although in a nonlinear fashion. This bar behaviour is also

reproduced by the simulation of the real-life event (fourth panel of Figure 15), although it was characterized by almost concomitant river discharge and sea storm. The water river jet eroded the most upriver bar crest (black arrow in the fourth panel of Figure 15) while an accretion has been observed in the seaward area, likely also impacted by the simultaneous wave action. The results of the numerical simulations confirmed that the effect of the river forcing is maximum on the portion of the bar located most upriver and almost null on the most downriver crest, which was not eroded either in the parametric or in the real-life simulations. Moreover, in the latter case, the simultaneous action of the waves did not significantly reduce the effect of the river discharge on the most upriver bar crest because it was located about 110 m upstream from the river mouth. For that case, the erosion of the bar crest was similar to that of the parametric simulation with $Q=100 \text{ m}^3/\text{s}$, although the discharge was lower. This suggests that the waves did not greatly oppose the action of the river.

When the river action was weak, the estuary dynamics was dominated by the sea action. The concurrent effect of storm surge and high tide triggered a quick upriver migration of the bar as observed during the event of March 2018 (red box in Figure 9a). The storm was associated with increasing sea and river water levels, up to 0.6 m and 2 m, respectively. These overall conditions are similar to those reported by [Melito et al. \(2020\)](#) for an event that occurred in January 2014. [Melito et al. \(2020\)](#) largely focused on the upriver propagation of infragravity (IG) waves and demonstrated that: (i) moving upriver of the mouth IG waves gained a more relevant role over swell and wind waves and the IG band experienced the largest increment in flux energy density into the river; (ii) the tide has an important role in controlling the upriver propagation of IG waves, enhancing such modes during flood and high tide, mainly because of an increase of water levels into the estuary. In particular, during the January 2014 event IG waves travelled upriver at estimated velocities between 3.6 m/s and 5.5 m/s during an intense storm and propagated up to 600 m into the river channel, i.e. slightly upriver of the location where the bar of interest was located. In view of the above, we argue the event that occurred in March 2018 caused the upriver migration of the bar and that IG waves contributed to the overall dynamics of the bar. In the last 6 days of March 2018, the y-coordinate of the bar centre of mass moved from about 8 m to about 39 m, thus the bar experienced a migration of more than 30 m upriver or 1.2 river widths. The real-life numerical simulation confirmed the primary role of waves on sediment deposition just inside the river mouth and the upriver migration of the bar crests (black arrows in the second panel of Figure 15). It showed an upriver migration of the most downriver bar crest of about 1 river width, i.e. slightly less than the observed one. Moreover, the real-life simulation also confirmed that small storms, like that occurred on 31 March 2018, characterized by wave significative height of less than 0.8 m and coming from the E, were able to slowly and slightly model the shape of the bar. The effect of waves coming from different directions was inspected through parametric simulations (bottom panel of Figure 14) confirming that 10-years return period NNE waves, approaching the coast perpendicularly to the estuary, had the largest effect on the upriver migration of the bar, causing a displacement of the most seaward bar crest of one river width. Easterly waves produced instead an upriver displacement of such bar crest smaller than one river width. Moreover, NNE waves modified also the most upriver bar crest, inducing an upriver migration smaller than one river width. Differently from the discharge-only cases, wave-only cases showed no variation of the riverbed level upstream of the bar, suggesting that the waves enter the estuary, break on the bar producing upriver sediment transport and then lose most of their energy, no longer being able to modify the riverbed farther upstream. In addition to the action of storm waves, which caused fairly rapid upriver displacements of the bar, a slow upriver migration of the bar also occurred under a mild wave climate, as

was observed in March-April 2017 or April 2018. While pushing sediment upriver, the waves modify the configuration of the bar (Mikhailov, 1966) and give rise to complex morphodynamic shapes as observed from the images in August and September 2019. Figure 9b shows the bar emerging in December 2018 about 77 m farther upriver than where it had disappeared in June 2018, after a period characterized by moderate wave climate (maximum wave height about 2 m) and absence of river discharge.

Both field observations and numerical simulations did not highlight a direct impact of the tide on the dynamics of the bar, but the size and the shape of the emerged part of the bar are strongly linked to the cyclic tide variation. This was confirmed by the hourly variations of the emerged portion of the bar that have not been discussed here because we were interested in longer time scales and therefore, we took a mean datum per day. However, if we consider the total sea water level variation, its effect can be seen in several cases. For example, measurements and visual observations of the images show that in the interval 2018 – 2019 the bar was always present in the estuary, but it was sometimes submerged by the high sea water level (e.g. from July 2018 to December 2018). Moreover, the sea water level variation effect was particularly evident in February 2019 when the area of the most downstream bar experienced its highest increase, about 12 times. The growth was most likely attributed to the decrease of the sea water level from about 0.2 m to about -0.5 m. On the contrary, in November 2019, both river and sea water levels increased, leading to a sharp decrease of the bar area of about 19 times. Since the study environment was characterized by small tidal variation, we argue that the main factors that govern the dynamics of the MR bar are the river discharge, wave forcing, and their interaction. The extent of bar migration and the place where the bar forms are strongly dependent on the intensity of the river current-wave interaction. For example, if two bars were located at approximately the same distance from the mouth and they were hit by similar river discharges, the bar that would experience the highest downriver displacement would be that subject to the minor simultaneous wave action. Moreover, when the bar is located farther upstream, it is more influenced by the action of the river flow. On the contrary, when the bar is located more seaward, the river flow has less impact than the waves on its migration. In the period when there were two distinct mounds (spring 2019), the most downriver one was more subjected to the wave action than the most upstream one, which appeared to be sheltered by the downriver bar. However, it was not possible to observe that the most upriver bar protected the most downriver one from the river action, because no significant discharge occurred when there were two distinct bars visible. In fact, the discharges of May 2019 happened when the bars had formed a single deposit.

5. Conclusions

We conducted a novel analysis of the dynamical evolution of a river, inner mouth bar within a microtidal estuary. Images collected by fixed cameras were used to describe the evolution of the bar and image processing operations were performed to detect the bar location and extrapolate its geometric characteristics (i.e. area and centre of mass). The collected information was then correlated with the available data of the main forcing involved in the morphodynamics of the estuary to understand their role in the evolution and migration of the bar. The upriver migration of the bar can be explained by both the action of waves and the growth of the bar followed by the shift of the centre of mass. Conversely, peaks in river water level and discharge lead to the submersion of the bar and to its downriver migration. Parametric simulations confirmed that the downriver displacements of the bar, due to 1-year return period river discharges, are in the order of four river widths, while upriver migrations due to 10-years return period waves are in the order of one river width,

with waves approaching the estuary perpendicularly causing the highest bed level change. The simulation of the real-life event was performed to reproduce one of the more complex time periods (March 2018), which was characterized by a downriver bar migration followed by an upriver one. Simulation results confirmed the role of the river discharge on the erosion of the bar and consequent downriver deposition and that of the waves on the upriver migration of the crests of the deposit. The effect of the tide on the hourly change of the area of the bar has not been discussed in the present study, since it obviously leads to a reduction or increase of the visible area during high or low tide, respectively. The tide was also found to affect the emerged area of the bar on the time scale of this study (3 years). An overall increase or decrease of the tidal level produced a reduction (November 2019) or a rise (February 2019) of the visible area of the bar. Moreover, the results of the numerical simulation confirmed that the tide, known to positively modulate the upriver propagation of IG waves, has a marginal influence on the morphodynamics of the MR estuary.

In summary, both observations and numerical simulation, suggest that bar formation and evolution is controlled by the sediment made available by the river flow and the main forcing of river discharge, wave intensity and tide modulation. Strong river discharges naturally transport sediments out to sea, which results in downriver sediment transport and migration of the bar. Sea waves (tide-modulated IG waves included) are responsible for the upriver sediment transport and migration of the bar. All collected evidence suggests that even moderate river discharges (comparable to the 1-year return period conditions) force a downriver bar migration stronger than the upriver migration induced by intense storm waves (comparable to the 10-years return period). When the typical yearly cycle of summertime deposition (low river discharges) and wintertime erosion of sediments out of the river mouth is interrupted by long periods of droughts, an inner bar is generated and may persist for years. Recent droughts have led to the emergence of the bar observed for over 3 years starting in 2017 and highlights the pivotal role of precipitation and river discharge.

The video monitoring station allows the analysis at both short (hours) and long (years) time scales. It provides high-resolution images and videos that can be post-processed to study both the emerged and submerged morphology, along with the hydrodynamics of the MR estuary. Additionally, the coupling of video data with numerical modelling may be used to address fundamental questions at the MR estuary such as: What is the minimum river discharge needed to flatten the bar and transport river bar sediments out to sea? Can numerical simulations be used to correctly reproduce the role of tide-modulated IG waves on the mouth sediment transport?

CRedit authorship contribution statement

Agnese Baldoni: Conceptualization, Methodology, Software, Formal analysis, Investigation, Data curation, Writing - original draft, Visualization. **Eleonora Perugini:** Conceptualization, Methodology, Software, Formal analysis, Data curation, Writing - review & editing. **Luciano Soldini:** Data acquisition, Conceptualization, Writing - review & editing, Supervision. **Joseph Calantoni:** Conceptualization, Writing - review & editing, Funding acquisition. **Maurizio Brocchini:** Conceptualization, Writing - review & editing, Supervision, Funding acquisition.

Declaration of competing interest

The authors declare that they have no known competing financial interests or personal relationships that could have appeared to influence the work reported in this paper.

Acknowledgments

The financial support from the Office of Naval Research Global (UK) MORSE Project (Research Grant N62909-17-1-2148) and from the Fondazione Cariverona 2019 PhD scholarship “Osservazione e MODellazione dell'idromorfoDINamica estuarina e costiera (OSMODIN)” (2019.0294 - D.R. n. 603 of 28.05.2019) is gratefully acknowledged. J. C. was supported under base funding to the U.S. Naval Research Laboratory from the Office of Naval Research. The authors would like to thank their colleagues who made significant contributions during the planning and execution of the field experiment including Edward F. Braithwaite III, Alex Sheremet, Allen Reed, Margaret L. Palmsten. Additionally, the authors would like to thank the following authorities: the Municipality of Senigallia, the Capitaneria di Porto of Senigallia and of Ancona, MARIDIPART La Spezia and MARIFARI Venezia. Acknowledgments go also to: GESTIPOINT (Senigallia), Club Nautico (Senigallia), NOTA srl (Senigallia), Carmar Sub (Ancona), Sena Gallica (Senigallia), METIS S.R.L. (Senigallia).

References

- Anthony, E.J., 2015. Wave influence in the construction, shaping and destruction of river deltas: a review. *Marine Geology* 361, 53–78. <https://doi.org/10.1016/j.margeo.2014.12.004>
- Blondeaux, P., Seminara, G., 1985. A unified bar-bend theory of river meanders. *Journal of Fluid Mechanics* 157, 449–470. <https://doi.org/10.1017/S0022112085002440>
- Brocchini, M., 2020. Wave-forced dynamics in the nearshore and river mouths, and swash zones. *Earth Surface Processes and Landforms* 45(1), 75–95. <https://doi.org/10.1002/esp.4699>
- Brocchini, M., Calantoni, J., Postacchini, M., Sheremet, A., Staples, T., Smith, J., Reed, A.H., Braithwaite, E.F., Lorenzoni, C., Russo, A., Corvaro, S., Mancinelli, A., Soldini, L., 2017. Comparison between the wintertime and summertime dynamics of the Misa River estuary. *Marine Geology* 385, 27–40. <https://doi.org/10.1016/j.margeo.2016.12.005>
- Canestrelli, A., Nardin, W., Edmonds, D., Fagherazzi, S., Slingerland, R., 2014. Importance of frictional effects and jet instability on the morphodynamics of river mouth bars and levees. *Journal of Geophysical Research – Oceans* 119, 509–522. <https://doi.org/10.1002/2013JC009312>
- Chawla, A., Kirby, J.T., 2002. Monochromatic and random wave breaking at blocking points. *Journal of Geophysical Research – Oceans* 107, 3067. <https://doi.org/10.1029/2001JC001042>

1 CMEMS, Copernicus. https://resources.marine.copernicus.eu/?option=com_csw&view=details&product_id=MEDSEA_HINDCAST_WAV_006_012

2 Colombini, M.; Seminara, G.; Tubino, M., 1987. Finite-amplitude alternate bars. *Journal of Fluid Mechanics* 181, 213–232. <https://doi.org/10.1017/S0022112087002064>

3 Dalrymple, R.W., Choi, K., 2007. Morphologic and facies trends through the fluvial–marine transition in tide-dominated depositional systems: A schematic framework for
4 environmental and sequence-stratigraphic interpretation. *Earth Science Reviews* 81(3–4), 135–174. <https://doi.org/10.1016/j.earscirev.2006.10.002>

5 Deltares, 2014. Delft3D-Flow, Simulation of multi-dimensional hydrodynamic flows and transport phenomena, including sediments, User Manual, Version 3.15.34158, May
6 2014, 684 pp.

7 Deltares, 2019. Delft3D-Wave, Simulation of short-crested waves with SWAN, User Manual, Version 3.05.58426, May 2019, 200 pp.

8 DHI Report, 2020. Dinamica della sedimentazione marina e impatto sulla costa.

9 Edmonds, D. A., and Slingerland, R. L., 2007. Mechanics of river mouth bar formation: Implications for the morphodynamics of delta distributary networks. *Journal of*
10 *Geophysical Research* 112, F02034. <https://doi.org/10.1029/2006JF000574>

11 Fagherazzi, S., Edmonds, D.A., Nardin, W., Leonardi, N., Canestrelli, A., Falcini, F., Jerolmack, D.J., Mariotti, G., Rowland, J.C., Slingerland, R.L., 2015. Dynamics of
12 river mouth deposits. *Reviews in Geophysics* 53 (3), 642–672. <https://doi.org/10.1002/2014RG000451>

13

14 Falcini, F., Piliouras, A., Garra, R., Guerin, A., Jerolmack, D.J., Rowland, J., Paola, C., 2014. Hydrodynamic and suspended sediment transport controls on river mouth
15 morphology. *Journal of Geophysical Research - Earth Surface* 119 (1), 1–11. <https://doi.org/10.1002/2013jfr002831>

16

17 Favali, P., Frugoni, F., Monna, D., Rainone, L., Signanini, P., Smriglio, G., 1995. The 1930 earthquake and the town of Senigallia (Central Italy): an approach to seismic risk
18 evaluation. In: Boschi, E., et al. (Eds.), *Earthquakes in the Past: Multidisciplinary Approaches*, *Annali di Geofisica* XXXVIII (5–6), pp. 679–689.

19

20 Hayes, M.O., 1980. General morphology and sediment patterns in tidal inlets. *Sedimentary Geology* 26, 139–156. [https://doi.org/10.1016/0037-0738\(80\)90009-3](https://doi.org/10.1016/0037-0738(80)90009-3)

21

22 Hartley, R., & Zisserman, A., 2003. *Multiple view geometry in computer vision*, Cambridge University Press. <https://doi.org/10.1017/CBO9780511811685>

23

24 Holman RA, Stanley J., 2007. The history and technical capabilities of Argus. *Coastal Engineering* 54, 477–491. <https://doi.org/10.1016/j.coastaleng.2007.01.003>

25 Holman, R., Haller, M. C., 2013a. Remote sensing of the nearshore. *Annual Review of Marine Science* 5, 95–113. <https://doi.org/10.1146/annurev-marine-121211-172408>

26 Holman, R., N. Plant, and T. Holland, 2013b, cBathy: A robust algorithm for estimating nearshore bathymetry. *Journal of Geophysical Research – Oceans* 118, 2595–2609.
27 <https://doi.org/10.1002/jgrc.20199>

28 Lan, P.T., Son, T.S., Gunasekara, K., Nhan, N.T., Hien, L.P., 2013. Application of Remote Sensing and GIS technology for monitoring coastal changes in estuary area of the
29 Red river system, Vietnam. *Journal of the Korean Society of Surveying, Geodesy, Photogrammetry and Cartography* 31 (6-2), 529–538.
30 <http://dx.doi.org/10.7848/ksgpc.2013.31.6-2.529>.

31 Melito L.; Postacchini, M.; Sheremet, A.; Calantoni, J.; Zitti, G.; Darvini, G.; Brocchini, M., 2020. Hydrodynamics at a Microtidal Inlet: Analysis of Propagation of the Main
32 Wave Components. *Estuarine Coastal and Shelf Science*. <https://doi.org/10.1016/j.ecss.2020.106603>

33 Mikhailov, V. N., 1966. Hydrology and formation of river-mouth bars. In: *Scientific Problems of the Humid Tropical Zone Deltas and Their Implications*, UNESCO, Paris,
34 1, 59–64.

35

36 Olabarrieta, M., Geyer, W.R., Kumar, N., 2014. The role of morphology and wave-current interaction at tidal inlets: an idealized modeling analysis. *Journal of Geophysical*
37 *Research – Oceans* 119 (12), 8818–8837. <https://doi.org/10.1002/2014JC010191>

- 1 Perugini, E., 2019. The Application of Video-Monitoring Data to Understand Coastal and Estuarine Processes. PhD Thesis, Università Politecnica delle Marche.
2 <http://hdl.handle.net/11566/263695>
- 3 Perugini, E., Soldini, L., Palmsten, M., Calantoni, J., Brocchini, M., 2018. A new video monitoring station along the Adriatic Coast. XXXVI Convegno Nazionale di Idraulica
4 e Costruzioni Idrauliche, IDRA2018, Ancona, Italy, 12-14 September 2018.
- 5 Perugini, E., Soldini, L., Palmsten, M.L., Calantoni, J., Brocchini, M., 2019. Linear depth inversion sensitivity to wave viewing angle using synthetic optical video. Coastal
6 Engineering, 152. <https://doi.org/10.1016/j.coastaleng.2019.103535>
- 7 Pianca, C., Holman, R., Siegle, E., 2014. Mobility of meso-scale morphology on a microtidal ebb delta measured using remote sensing. Marine Geology 357, 334–343.
8 <https://doi.org/10.1016/j.margeo.2014.09.045>
- 9 Rolandi, G., Paone, A., Di Lascio, M., Stefani, G., 2008. The 79 AD eruption of Somma: the relationship between the date of the eruption and the southeast tephra dispersion.
10 Journal of Volcanology and Geothermal Research 169 (1), 87–98. <https://doi.org/10.1016/j.jvolgeores.2007.08.020>
- 11
- 12 Takewaka, S., 2016. Observation of Whole Flushing Process of a River Sand Bar by a Flood Using X-Bad Radar. Journal of Marine Science and Engineering 4 (32).
13 <https://doi.org/10.3390/jmse4020032>
- 14
- 15 Valle-Levinson, A. (Ed.), 2010. Contemporary Issues in Estuarine Physics. Cambridge University Press. <http://dx.doi.org/10.1017/CBO9780511676567>
- 16
- 17 van der Wegen, M., 2010. Modeling morphodynamic evolution in alluvial estuaries. CRC Press.
- 18
- 19 Witting, M., Wehmeyer, C., & Niemeyer, H. D., 2010. Medium-term morphodynamic modeling of mixed mud and sand in the tidal basin Jadebusen. Coastal Engineering
20 Proceedings, (32), 65-65. <https://doi.org/10.9753/icce.v32.sediment.65>
- 21
- 22 Wright, L., 1976. Morphodynamics of a wave-dominated river mouth. Coastal Engineering Proceedings, 1 (15), 99. <https://doi.org/10.9753/icce.v15.99>
- 23
- 24 Zuiderveld K., 1994. Contrast Limited Adaptive Histogram Equalization. In: P.S. Heckbert (Eds.), Graphics Gems IV. Academic Press, pp. 474-485.
25 <https://doi.org/10.1016/B978-0-12-336156-1.50061-6>
- 26
- 27
- 28